TÉCNICO LISBOA

Development of an automatic 2D-3D image matching method for reproducing three-dimensional humeral positions using single and dual plane fluoroscopy

Filipa Pinto Leal

Thesis to obtain the Master of Science Degree in

Biomedical Engineering

Supervisors: Prof. Carlos Miguel Fernandes Quental

Prof. João Orlando Marques Gameiro Folgado

Examination Committee

Chairperson: Prof. Ana Luísa Nobre Fred

Supervisor: Prof. Carlos Miguel Fernandes Quental

Members of the Committee: Prof. Rui Miguel Barreiros Ruben

November 2018

Agradecimentos

Antes de mais, gostaria de agradecer ao Professor Carlos Quental e ao Professor João Folgado, os meus orientadores, por todo o acompanhamento e paciência que demontraram em todas as fases deste trabalho.

Um obrigada sincero às minhas cinco amigas que conhecí no técnico: Joana Pinto, Marta Conceição, Rafaela Saraiva, Rita Oliveira e Teresa Bucho. Obrigada por terem tornado este percurso muito mais prazeroso, por não me deixarem sentir sozinha e fazerem com que eu demonstre sempre o melhor de mim quando estou com vocês.

Quero agradecer aos meus amigos de sempre, ao António, à Catarina e à Lisa por tudo o que me ensinaram e por me demontrarem que a amizade perdura no tempo.

Quero agradecer à Eduarda por tudo e por mais alguma coisa: pela paciência sem fim, pelo apoio e por estar sempre à distância de uma chamada quando eu mais preciso.

Por último, deixo um enorme agradecimento aos meus pais a quem eu devo tudo aquilo que sou hoje. Quero agradecer à minha mãe pelo apoio incansável, por me arranjar mil e uma formas de me incentivar e, acima de tudo, por pensar sempre em mim e não deixar que me falte nada. Ao meu pai quero agradecer o amor incondicional e o espirito de sacríficio e responsabilidade que me proporcionaram esta experiência.

Abstract

The shoulder is a complex system with high clinical relevance. Fluoroscopic image-model techniques have been widely used due to its reported sub-millimeters levels of accuracy. In this study, an automatic 2D-3D image-model matching method was developed to reproduce humerus spatial positions using either dual and single fluoroscopic images. The matching method was accomplished through an optimization process and validated under an idealized an *in vivo* environment. By limiting the search space of the optimizer to a range of $[\pm 5\,°; \pm 5\,mm]$ and $[\pm 20\,°; \pm 20\,mm]$ from the ideal pose, three objective functions considering simple and complex humerus poses were tested. Using dual fluoroscopic images, the results showed that the minimization of the distances was the objective function which reproduced both type of humerus poses with more accuracy and in agreement with previous studies. The minimization of the areas and moments of inertia showed limited accuracy. Satisfactory results were obtained under the search space of $[\pm 5\,°; \pm 5\,mm]$, while under the range of $[\pm 20\,°; \pm 20\,mm]$ less accurate results were obtained. When using single fluoroscopic images, the in-plane accuracy was satisfactory, but at the expense of large out-plane errors. A qualitative analysis of the method under *in vivo* conditions showed poor results. Using the respective fluoroscopic images and 3D models, this method can also be applied to the clavicle and the scapula geometry. In the future, this method can be used to study the shoulder kinematics.

Keywords

Dual plane, Fluoroscopic image, Kinematics, Optimization, Single plane, Shoulder

Resumo

O mecanismo do ombro é um sistema complexo e de elevada importância clínica. A aplicação de técnicas de fluoroscopia para analisar a cinemática do ombro tem demonstrado resultados bastante promissores. Um método automático para determinar posições tridimensionais do úmero usando imagens de fluoroscopia biplanar e uniplanar foi desenvolvido. Este método tem por base técnicas de optimização, tendo sido validado em condições reais e ideais. O espaço de procura do optimizador foi limitado para um intervalo de ± 5 ° na rotação e $\pm 5\ mm$ na rotação e um intervalo de ± 20 ° e $\pm 20\ mm$ a partir da posição ideal. Para cada um destes intervalos, três funções objetivo foram testadas considerando posições simples e complexas do úmero. Usando imagens ideais de fluoroscopia biplanar, os resultados mostraram que a minimização das distâncias foi a função objetiva que demonstrou maior precisão na determinação das posições do úmero. A função objetivo da minimização das áreas e dos momentos de inércia demonstraram precisão limitada. Para um espaço de procura de ± 5 ° e $\pm 5\ mm$, os resultados obtidos foram satisfatórios, enquanto que para o espaço de procura ligeiramente maior, ± 20 ° e $\pm 20\ mm$, resultados menos precisos foram obtidos. Com imagens ideias de fluoroscopia uniplanar, os erros obtidos no plano de projeção foram satisfatórios, enquanto que fora do plano de projeção elevados erros foram registados. Numa análise qualitativa do método usando imagens de fluoroscopia reais, resultados pouco precisos foram obtidos. Apesar deste método ter sido aplicado apenas à geometria do úmero, a clavícula e a omoplata também poderão ser estudados desde que as respetivas imagens de fluoroscopia e modelo 3D sejam providenciadas.

Palavras-Chave

Biplanar, Cinemática, Imagens de fluoroscopia, Ombro, Optimização, Uniplanar

Table of Contents

List of Figures

List of Tables

List of Acronyms

2D	Two-dimensional
3D	Three-dimensional
6DOF	Six degree-of-freedom
AC	Acromioclavicular
CT	Computed Tomography
CAD	Computed aided drafting
DFIS	Dual fluoroscopic imaging system
GH	Glenohumeral
GT	Greater tuberosity
MRI	Magnetic resonance imaging
RGP	Random generated poses
ROI	Region of interest
SIS	Subacromial impingement syndrome
SC	Sternoclavicular
ST	Scapulothoracic
SP	Simple poses

Chapter 1

Introduction

1.1 Motivation and Goals

The shoulder is the most complex system consisting of three bones (scapula, humerus, clavicle), four joints (glenohumeral, scapulothoracic, acromioclavicular, and sternoclavicular) and a vast number of surrounding tendons and ligaments [3]. The coordinated actions in all articulations give the shoulder mechanism the widest range of motion of all human body [4]. Such large flexibility comes at the cost of intrinsic joint stability being the shoulder joint, the most frequently dislocated joint in the human body [4]. Therefore, it is notorious that the accurate determination of the human shoulder kinematics is a challenging issue in biomedical engineering.

The determination of the kinematics of the shoulder mechanism is crucial to better understand numerous pathologies. For example, altered kinematics of the scapula have been reported in patients with shoulder impingement syndrome [5, 6, 7] Also, glenohumeral dysfunctions in translation and external rotation of the humeral head on the glenoid have been observed in population with glenohumeral instability [3, 8].

Conventional methods have relied on the use of surface markers. This technique has revealed to be inaccurate for measuring scapula motion due to its flat shape, soft tissue covering and its significant subcutaneous motion [19]. This technique has also revealed to be inadequate for the humerus, since the glenohumeral joint center, important to define its longitudinal axis, is not a palpable bony landmark, and thus has to be estimated [4]. Other techniques have used direct insertion of pins to measure shoulder kinematics, especially the clavicle. As the clavicle only has two bony landmarks, its axial rotation cannot be calculated through non-invasive techniques. Therefore, new techniques to accurately determine the shoulder kinematics need to be developed.

The main objective of this work is to develop a method capable of measuring the humerus kinematics and that can be applicable to the clavicle and the scapula, so that in the future an analysis of the shoulder kinematics can be performed. This study applies fluoroscopic image-model registration techniques to determine humerus positions in space. These techniques have been widely used with successful results demonstrated [2, 9, 10].

1.2 Thesis Outline

The current work is divided into six chapters. The first chapter, which includes this section, is an introductory chapter that describes the motivation and main goals of this work.

In Chapter 2, the shoulder complex anatomy and main shoulder pathologies are described. This chapter also includes a description of the techniques used to measure shoulder kinematics. This chapter ends with a brief introduction to the optimization algorithm used in this study.

Chapter 3 describes in detail the methodology followed in this study. It describes the automatic 2D-3D matching method developed, including the segmentation and reconstruction of the 3D humerus model, the developed optimized matching algorithm and respective objective functions tested. This chapter also explains how the method was validated.

Chapter 4 presents the results obtained with the method developed. The first section consists on a quantitative analysis of the accuracy of the method under an idealized testing environment. The second subsection reports a qualitative analysis of the accuracy of the method with an *in vivo* environment test.

In Chapter 5, the results obtained are discussed. The strengths and limitations of this study are also addressed.

Finally, in Chapter 6, the main conclusions of this study and some suggestions for future developments in this area are presented.

Chapter 2

Background Concepts

For a detailed kinematic analysis of human shoulder, a broader knowledge about its anatomy is essential. Given the complex anatomy and biomechanics which characterizes the human shoulder, its mechanism has not been so intensively studied as the mechanism of the knee and the hip. In this chapter, key anatomical concepts of the shoulder complex are firstly presented. Then, a description of the conventional and current methods used to measure shoulder kinematics are introduced. At last, a brief explanation of the optimization algorithm used in this study is presented.

2.1 Shoulder Anatomy

This section is divided into three subsections each dedicated to a different structure of the shoulder complex: (1) the osteology and (2) the joints.

2.1.1 Osteology

The shoulder complex is formed by the bones of the shoulder girdle (clavicle and scapula), the humerus, sternum and rib cage. These bones form four joints such as the glenohumeral, acromioclavicular, sternoclavicular and scapulothoracic. These structures are surrounded by several muscles forces and ligaments which act as static and dynamic stabilizers of the shoulder joint [40].

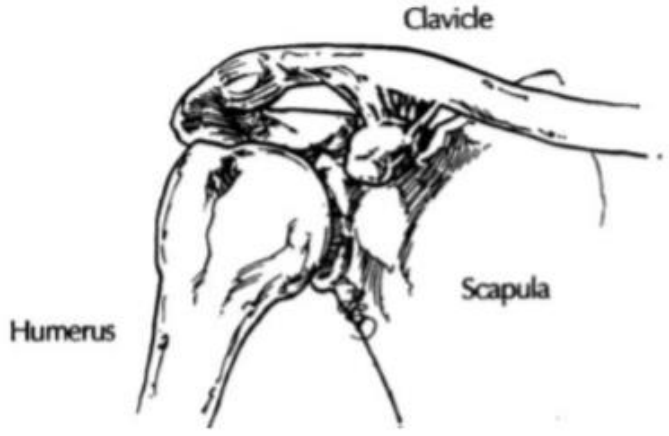

Figure 2.1 – Bony structure of the shoulder complex [1] .

2.1.1.1 Clavicle

The clavicle is the bony structure which articulates with the sternum medially, forming the sternoclavicular joint, and connects the upper extremity to the axial skeleton [40]. It also articulates with the acromion of the scapula laterally, forming the acromioclavicular joint.

The clavicle is described as a long bone with an S-shaped curvature. It has a shaft and two extremities: the sternal and acromial extremity. The shaft is gently curved with convexity forwards in its medial two-thirds and concavity forwards in its lateral third [39]. As represented in Figure 2.2, several muscles which contribute to shoulder motion are attached to the clavicle, such as the deltoid, trapezius and pectoralis [41].

Figure 2.2 – Posterior view of the clavicle and respective muscle attachments [39]

2.1.1.2 Scapula

The scapula is a flat and triangular bone and is represented in Figure 2-3 A. The scapula lies on the posterolateral aspect of the thoracic cage and, when in its resting position, covers the second to seventh rib [40]. This bone has a bony ridge, called the spine of the scapula, that extends superiorly and laterally to form the base of the acromion [40]. The acromion, a large and somewhat triangular process, articulates with the clavicle, forming the acromioclavicular joint. On the lateral angle of the scapula is a shallow cavity called glenoid fossa, as represented in Figure 2-3 B. The glenoid fossa is an important part of scapula which articulates with the humerus head forming the glenohumeral joint.

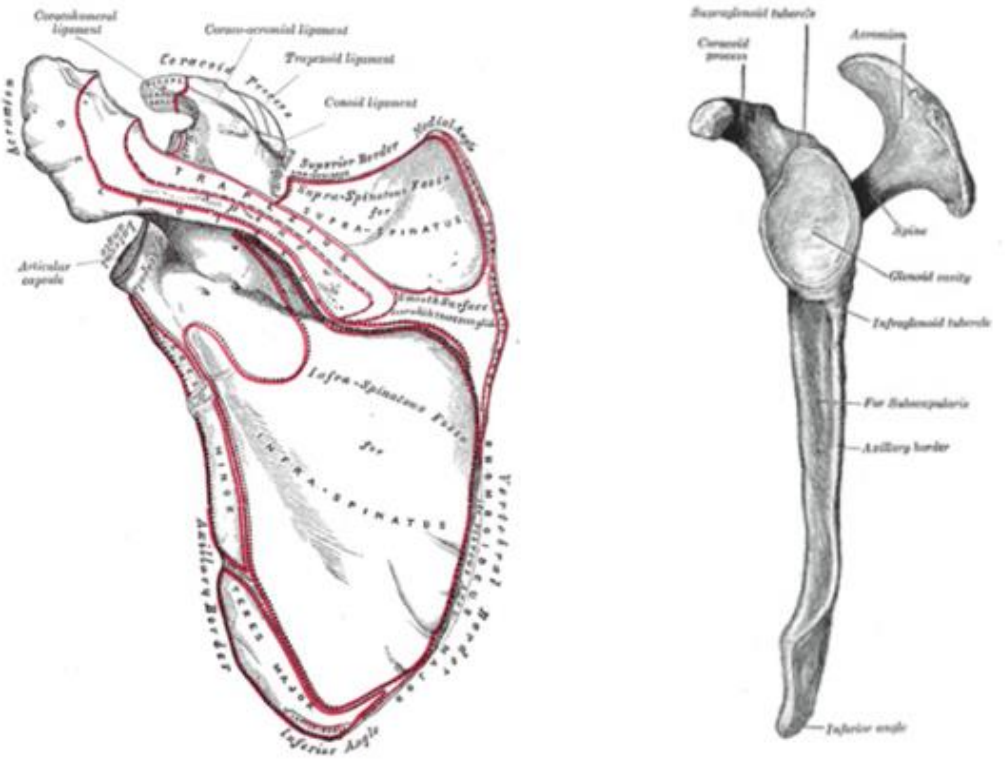

(a) (b)

FIgure 2.3 – Posterior (a) and lateral (b) view of the scapula [39]

2.1.1.3 Humerus

The humerus is the largest and longest bone of the human upper extremity [39]. It consists of three sections: the body and the upper and lower extremities. A detailed representation of this bone is presented in Figure 2.4.

The humeral upper extremity is constituted by a half spheroid-shaped head joined to the body by a constricted portion called anatomical neck, and two eminences, the greater and lesser tubercles [39]. The head, which articulates with the glenoid fossa of the scapula, is directed upward, medialward, and a little backward [39]. The anatomical neck makes an obtuse angle with the body of the humerus. The greater (GT) and lesser (LT) tuberosity are an attachment site for the rotator cuff tendons [40]. Supraspinatus, infraspinatus and teres minor tendon are attached on the GT, whereas subscapularis is attached on the LT. Below the tubercles is another constriction called surgical neck which is frequently fractured. The body is almost cylindrical in the upper half of its extent and prismatic and flattened below [39]. The lower extremity of the humerus is constituted by two epicondyles situated on the lateral and medial side, and two articular surfaces slightly separated. On the lateral portion of this articular surface is the capitulum, a smooth and rounded eminence which articulates with the cupshaped depression on the head of the radius. Above the front part of the capitulum is the radial fossa, a slight depression where

the anterior border of the head of the radius lays when the forearm is flexed. On the medial side of this articular surface is a grooved structure named trochlea which fits within the semilunar notch of the ulna. Above, are two important fossae separated from one another by a thin lamina of bone. The coronoid fossa, situated above the front part of the trochlea, receives the coronoid process of the ulna during flexion of the forearm. The olecranon fossa, a deep triangular depression above the back part of the trochlea, accommodates the ulna during full extension of the forearm [39].

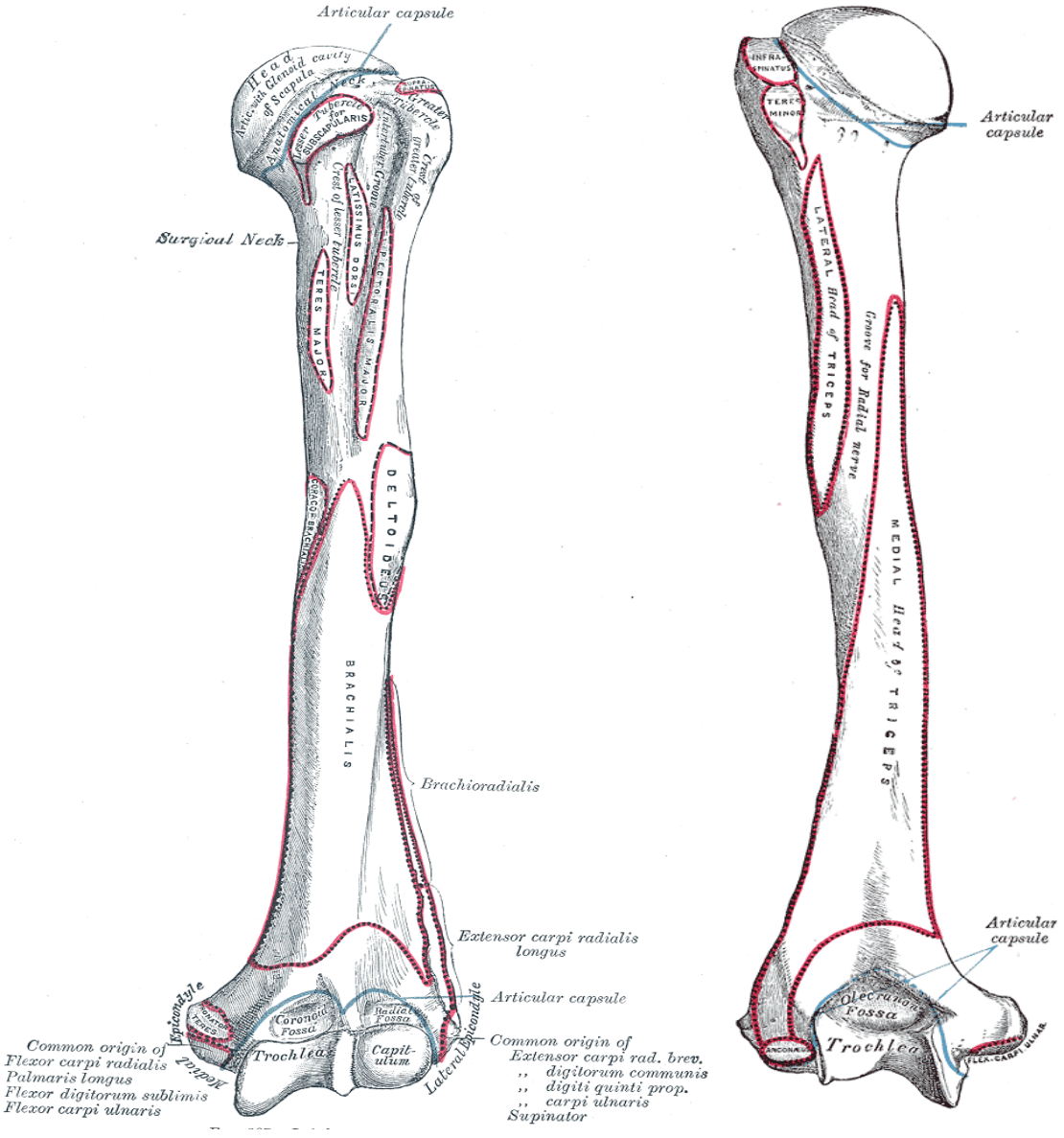

Figure 2.4 – Anterior view (a) and posterior view (b) of the left humerus [39]

2.1.2 Joints

The interaction between the bones of the shoulder complex results in four joints: the sternoclavicular (SC) joint, the acromioclavicular (AC) joint, the scapulothoracic (ST) joint, and the glenohumeral (GH) joint, commonly referred as shoulder joint in the literature.

2.1.2.1. Sternoclavicular Joint

The SC joint, represented in Figure 2.5, articulates the sternal end of the clavicle with the upper and lateral edge of the sternum as well as the cartilage of the first rib [40]. It is composed by a strong joint capsule, an articular disc, and three major ligaments - the costoclavicular ligament, the interclavicular ligament, and the anterior and posterior sternoclavicular ligaments. These ligaments are the most responsible for providing stability to the joint given the great disparity between the articular surface of the clavicle and the sternum [1]. The articular disk is a fibrocartilage interposed between the articulating surfaces of the sternum and clavicle that helps to distribute the forces between the two bones [40].

Under normal circumstances, this joint admits a limited range of motion in nearly every direction **-** elevation/depression, protraction/retraction and anterior/posterior rotation. When these movements occur, the clavicle in its motion carries the scapula with it, making this bone gliding on the outer surface of the chest [39]. This joint is therefore the only point of articulation of the shoulder girdle with the trunk [39].

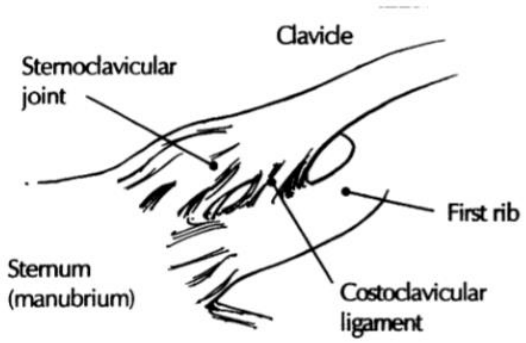

Figure 2.5 – Anterior view of the sternoclavicular joint [1]

2.1.2.2. Acromioclavicular Joint

The AC joint consists in the articulation between the acromial end of the clavicle with the medial margin of the acromion of the scapula [39]. It is constituted by a weak joint capsule, a fibrocartilage disc and two strong ligaments. The capsule surrounds the joint and is reinforced above and below by the superior and inferior AC ligaments [39]. The two strong ligaments are the superior and inferior AC ligaments and the coracoclavicular ligament. These ligaments function to suspend the scapula from the clavicle and to prevent posterior and medial motion of the scapula [40]. The disc separates the articular surfaces, undergoes rapid degeneration and is functionally absent by the fourth decade [1]**.**

The AC joint allows a gliding motion of the articular end of the clavicle on the acromion and the rotation of the scapula forward and backward upon the clavicle [39].

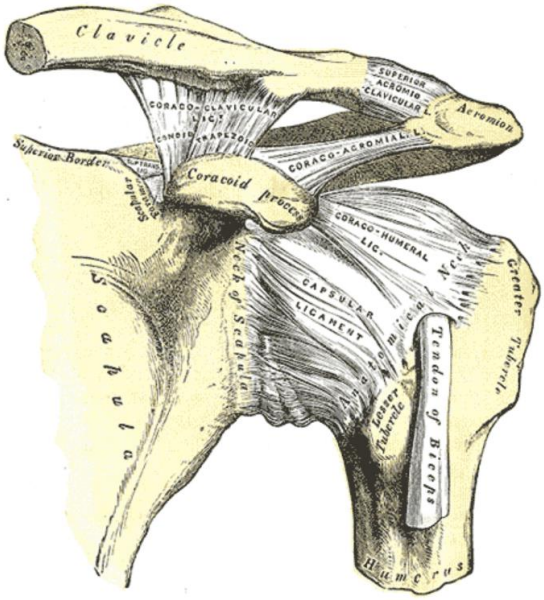

Figure 2.6 - Acromioclavicular joint with surrounding ligaments of the scapula [39]

2.1.2.3. Scapulothoracic Joint

The ST joint is not a true joint as there is no articular cartilage, synovium, or capsule, but a series of bursal and muscular planes [11]. The ST joint represents a space between the convex surface of the posterior thoracic cage and the concave surface of the anterior scapula [1]**.** This space is occupied by bursal and muscular structures which allow sliding of the scapula on the underlying thorax. Also, ST joint permits increased shoulder movement beyond the 120° offered only by the GH joint [1]**.** The ultimate functions of ST joint are to allow for proper positioning of the glenoid fossa for arm motion and to stabilize the scapula for efficient arm motion [40].

2.1.2.4. Glenohumeral Joint

The glenohumeral joint is a ball-and-socket synovial joint that results from the combination of the humeral head and the glenoid fossa of the scapula. This joint has the greatest range of motion of any joint in the body [40]. However, it is the least stable of them all, being very susceptible to dislocation and subluxation [40]**.** This instability derives from the fact that GH joint is described as an incongruous joint, this is, the head of the humerus and glenoid fossa barely make contact with each other at rest - at any given time, only 25% to 30% of the humeral head is in contact with the glenoid fossa [1]

The glenohumeral joint stability results from a strong interaction between passive and dynamic stabilizing structures. The passive constraints, where no active energy is required, include the glenohumeral capsule, ligaments and the glenoid labrum. By contrast, the dynamic constraints, include the shoulder complex musculature. Muscles play a dual role of support and motion. The muscles must maintain the proper alignment of the head of the humerus to the glenoid fossa as the arm is moving [40].

2.2. Shoulder pathologies

The big majority of the shoulder pathologies occur near the GH joint, therefore current research has focused on the movement patterns of the scapula and humerus [41]. In fact, clavicle motion has not been regularly studied as a potential mechanism of shoulder pathology due to difficulty capturing its dynamic motion *in vivo* [41].

The most frequent shoulder pathologies include shoulder impingement and associated rotator cuff disease, which can progress to rotator cuff tears as well as glenohumeral joint instability [12]. The majority of these shoulder complaints are related to occupational or athletic activities that involve frequent use of the arm at, or above, shoulder level [12].

Subacromial impingement syndrome (SIS) is the most common cause of shoulder pain [13]. SIS is defined as the repeated compression of the rotator-cuff muscles and tendons in the subacromial space, the interval between the coracoid-acromial arch, the antero-inferior part of the acromion and the humeral head [13].

The SIS aetiology can be attributed to anatomic abnormalities of the coracoacromial arch or humeral head; “tension overload”, ischemia, or degeneration of the rotator cuff tendons; and shoulder kinematic abnormalities [5]. Impingement is thought to be due to inadequate space for clearance of the rotator cuff tendons as the arm is elevated [5]. Regarding kinematic abnormalities, any motion that brings the greater tuberosity of the humerus closer to the coracoacromial arch is particularly problematic. These motions include excessive superior or anterior translations of the humeral head on the glenoid fossa, inadequate lateral (external) rotation of the humerus, and decreases in the normal scapular upward rotation and posterior tipping on the thorax, all occurring during humeral elevation [5].

Glenohumeral instability is defined as the inability to maintain the humeral head in the glenoid fossa [14]. Several studies have demonstrated dysfunctions in translation and external rotation of the humeral head on the glenoid in shoulders with glenohumeral instability [8, 14, 15].

Many problems, such as premature loosening of the glenoid component after shoulder arthroplasty or abnormal motion of the shoulder after rotator cuff reconstruction with tendon transfers, are not yet completely understood [16]. A dedicated analysis of the shoulder motion would help to understand these pathomechanisms and improve the sensitivity of clinical interventions (assessment, treatment and follow-up). Therefore, new methods able to accurately measure the *in vivo* shoulder motion are instrumental.

2.3 Techniques for measuring shoulder kinematics

This section starts with a review over the conventional approaches for measuring shoulder kinematics. A recent technique which has grown in popularity due to its high accuracy is described in detail last.

2.3.1 Conventional approaches

Conventional approaches for measuring the scapula, humerus and clavicle motion have relied upon the use of surface-mounted electromagnetic motion sensors, invasive techniques using bone pins, cadaveric simulations, 2D imaging and static 3D imaging. However, significant limitations are associated with each of these approaches.

Conventional motion measurement systems have relied on the use of video cameras to measure the position of surface markers. For example, Bagg et al. [17] evaluated the scapular rotation during arm abduction with a high-speed reflex cameras. Several surface markers were placed on specific regions of the scapula. When analysing the film, the markers were digitalized to measure the scapular humeral angle and estimated the position of its centre of rotation. Another conventional system is the use of an electromagnetic device to measure 3D movements, as performed by Johnson et al. [18] to analyse the scapula motion**.** This electromagnetic device is constituted by a transmitter which generates an electromagnetic field detected by the sensor attached to the skin. Both sensor and transmitter are connected to an electronics system which computes the relative position and orientation of the scapula in 6DOF [18]. However, skin-mounted sensors are highly susceptible to skin movement artefacts. The broad, flat shape, substantial soft-tissue covering, and the significant subcutaneous motion of the scapula makes it difficult to capture its motion with these surface sensors [19].

Another conventional technique used is the direct insertion of pins to measure shoulder kinematics. These techniques are usually used to measure the clavicle kinematics. In the clavicle, only two bony landmarks are palpable, making that its axial rotation cannot be calculated through non-invasive techniques [20]. To measure the scapular kinematics, McClure et al. [19] attached a motion sensor directly to the scapula with bone pins drilled into the spine of the scapula. Due to the invasive nature of this technique, a small sample of patients was used, which makes difficult to extrapolate conclusions to a broader population [19]. Likely, the use of pins became impractical since it can affect the movement of the volunteers and cannot be reliably secured in the same location [3].

Some approaches to track the motion of the scapula, humerus and clavicle have relied upon cadaveric simulations [3, 21, 22]. A dynamic shoulder testing apparatus has been developed to examine unconstrained glenohumeral joint motion in human cadaver% full upper extremities. Six computer-controlled hydraulic cylinders are used to simulate muscle action, while the corresponding tendon excursions and six-degree of freedom joint motion are measured. Trials showed that the testing apparatus creates highly reproducible glenohumeral joint motion in the scapular plane, The apparatus can be used to examine the function of the shoulder musculature during normal and pathologic motion at the glenohumeral joint. Ten human cadaveric shoulders were tested with a dynamic shoulder model simulating physiologic rotator cuff, deltoid, and biceps muscle forces. The combined effect of the muscle forces and acromial structure on subacromial impingement was measured with minimally invasive, miniature pressure transducers. Shoulders with large acromial spurs had significantly greater impingement pressures at the anterolateral acromion in neutral, internal, and external rotation compared with those with flatter acromia.

Application of a biceps muscle force reduced anterolateral acromial pressures by 10%. Failure to simulate a supraspinatus force decreased acromial pressure 52% in shoulders with type III acromia in neutral rotation. Without rotator cuff forces applied, the maximum deltoid muscle force required to elevate the arm increased by 17%. Acromial pressures were increased when no rotator cuff forces were applied, but the increases were not significant. After an anterior acromioplasty, pressures decreased by 99% anteriorly. However, failure to achieve a flat surface posteriorly increased pressures in this location, especially with the shoulder in external rotation. Modelling the rotator cuff and deltoid muscle forces demonstrated the importance of the muscular force couple to centre the humeral head during elevation of the arm. The inferior forces of the infraspinatus, teres minor, and subscapularis muscles were necessary to neutralize the superior shear force produced by the deltoid and supraspinatus muscles. These cadaveric experiments can provide high accuracy of bone position and motion, but are unable to accurately replicate the complex motions, muscles forces, or joint forces associated with dynamic in vivo conditions.

Planar analysis of joints is a common tool in clinical practice for evaluating pathological abnormalities and measuring both rotations and translations [23]**.** To measure shoulder complex kinematics, several *in vivo* analysis methods used radiographs at different levels of arm abduction [23]. However, given their static nature, these radiographs do not reflect a true motion pattern. Fluoroscopy, as a measure of dynamic joint motion**,** started to be used. Several studies reported the accuracy of this technique applied to the GH joint. For example, Pfirmann and colleagues developed a tracking method which automatically matches single plane fluoroscopy image sequences frame by frame [16]. This makes possible the identification of kinematic patterns of glenohumeral motion during abduction and adduction. However, these kind of 2D assessments are never a full kinematic analysis due to its insufficiency to characterize the translation of the joint in thee directions and rotation about thee axes.

A static 3D analysis of the humerus, clavicle and scapula position uses MRI [2, 15, 24, 25, 26]**,** CT [8] or dual plane radiography [27]. These imaging techniques combined with three-dimensional digital image postprocessing techniques permits to determine the orientation in 6DOF of the bone in relation to a fixed coordinate system. Though the three-dimensional information given by these techniques, they are still unable to assess dynamic motion.

Motivated by these limitations, new techniques have started to be developed, such as the fluoroscopic image-model registration techniques.

2.3.2 Fluoroscopic image-model registration technique

Fluoroscopy is a variation of radiography in which images are obtained in rapid succession and displayed in real time on a screen [28]. In its simple form, a fluoroscope consists of an X-ray source and a fluorescent screen, between which the patient is placed. Modern fluoroscopes include X-ray image intensifiers to improve image's visibility and project the resulting image on a monitor as a real-time image [24]. Fluoroscopy can be classified as single-plane or dual plane if one or two fluoroscopes are used, respectively.

Fluoroscopic imaging techniques have been increasingly explored due to its relatively low radiation dosage, accessibility of the equipment and their capacity to measure dynamic motion [9]**.** Various studies combined single fluoroscopic images with 3D bone models to determine joint positions in space. The scope of this measurement approach is to make that projected 3D bony models match 2D features of the acquired fluoroscopic image [9]. When the features of the two projections were considered to be matched, it is possible to obtain the relative poses of the 3D model in 6DOF.

A study of Li and colleagues [29] to quantify *in vivo* kinematics of the knee concluded that a dual plane fluoroscopy technique results in a higher accuracy than a single plane technique given its ability for measuring out-of-plane translation and rotation. Several studies started to use a dual fluoroscopic imaging system (DFIS) to study 6DOF joint kinematics. The joint is positioned in front of the two image intensifiers and imaged simultaneously by the fluoroscopes in order to acquire dual images of the joint [9, 30]. A DFIS to study the shoulder joint is represented in Figure 2.7. Now the match is performed between dual projections of the 3D model and the outlines of the respective components on both fluoroscopic images.

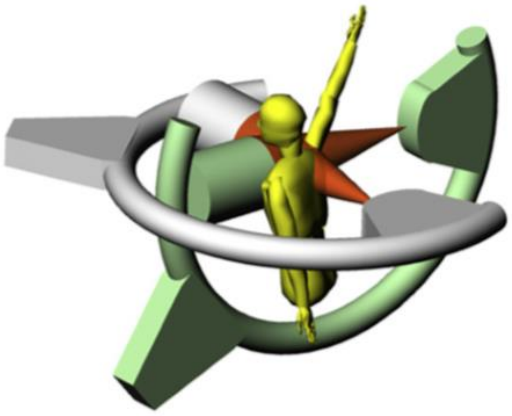

Figure 2.7 – Diagram of a DFIS for capturing the dynamic motion of the shoulder joint [2]

This methodology has been initially used to recreate the 6DOF motion of the knee joint. Hanson et al. [20] carried out a matching process by using a computer aided drafting (CAD) software which simulates the fluoroscopic environment and makes the manual adjustment of the positions and rotations of the 3D model so that its projection matches the fluoroscopic images. However, the manual matching procedure is laborious and can be a source of systematic errors and bias [9]. To overcome this limitation, J. Bingham and G. Li [9] implemented an optimized matching algorithm that automatizes the process. This method consists on the construction of a virtual replica of the DFIS. In a solid modelling program, two virtual source-intensifier pairs are introduced and oriented so that their relative locations replicate the geometry of the real fluoroscopic system [9]. The contours from the dual fluoroscopic images are placed on their respective virtual intensifiers. Then the 3D bone model is introduced into the virtual system and a

mathematical model is constructed so that the matching can start. The mathematical model consists on an optimization process which aims to minimize the distances between the 3D model projections and the outlines of the knee on the fluoroscopic images.

More recently, Massimini et al. [2] assessed the accuracy of using single and dual fluoroscopic images to study the shoulder joint kinematics in 6DOF using the same automatic matching algorithm as previous. Figure 2.4 represents an illustration of the virtual DFS created, where two virtual fluoroscopic imaging planes (F1 and F2) and two virtual cameras (S1 and S2) are positioned to represent the image intensifiers and the X-ray sources.

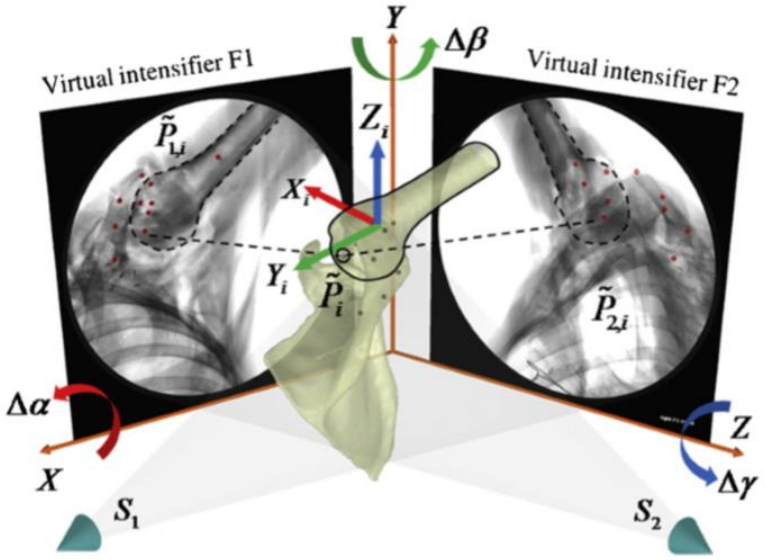

Figure 2.8 – An illustration of the virtual DFS used to reproduce the shoulder joint kinematics [2]

2.4 Computational Optimization Processes

Optimization methods are used extensively in biomechanics research to predict movement-related quantities that cannot be measured experimentally [31]. An example of this are the image matching optimization processes that have been performed to align implant and bone models to *in vivo* fluoroscopic images during dynamic movement [31]. Because optimization problems in biomechanics often have objective functions that are discontinuous, nonlinear, and possess many local optima, these problems can be very difficult to solve [32]. Gradient-based algorithms have been the most widely used to solve these kind of problems, primarily because of their rapid convergence properties – they use the derivative of the objective function to determine the most promising direction along which the algorithm should search [31]. However, gradient-based optimizers face important limitations. They are local rather than global by nature what make them sensitive to the initial guess. Convergence in gradient-based algorithms can be affected by

scaling to account for design variables with different length scales or units [31]. Furthermore, in most situations, the necessary gradient cannot be obtained analytically, and finite difference gradient calculations can be sensitive to the selected finite difference step size [31]. Motivated by these limitations, global optimizers, such as the case of genetic algorithms, has been increasingly used for biomechanical applications.

2.4.1. Genetic Algorithms

Genetic algorithms (GA) belong to the class of stochastic search optimization methods, which means that most of the computational steps of the algorithms are based on random number generation [44]. Due to its random nature, the genetic algorithm improves the chances of finding a global solution. Thus they prove to be very efficient and stable in searching for global optimum solutions. It helps to solve unconstrained, bound constrained, and general optimization problems, and it does not require the functions to be differentiable or continuous.

GA are based on Darwin's theory of natural selection and evolutionary biology. The basic idea of this approach is to start with a population of candidate solutions (called individuals). Each individual has a set of properties (called genome) traditionally represented in binary as strings of 0s and 1s (called genes). To each candidate solution is assigned a fitness value, usually the value of the objective function. From the current population, the more fit individuals are selected. The individual's genome is modified through random processes to form a new population. This new population is used in the next iteration of the algorithm. Since more fit individuals are used to create a new population, the successive populations have a higher probability of having individuals with better fitness values, and thus with the best solution for the problem [44]. Even though the stochastic methods do not offer an absolute guarantee of finding a global optimum, the probability of finding it increases as the population size and the number of times the algorithm is run increases [44].

These random processes mimic some genetic operations. The two genetic operators are: crossover and mutation. In the crossover operator, also called recombination, two individuals of the population are chosen so that its genes (sets of 0s and 1s) can be exchanged among themselves [33]. Mutation safeguards the process from a premature convergence and maintains diversity within the population [44]. In terms of a binary string, this step corresponds to selection of a few individuals of the population, determining a location on the strings at random, and switching the 0 to 1 or vice versa [44]. These processes are repeated for successive generations of the population until no further improvement in fitness is attainable. The individual in the final population with the highest fitness value is taken as the optimum solution.

Chapter 3

Computational Modelling Pipeline

The development of an automatic 2D-3D image matching method to determine humerus positions in 6DOF follows an extensive pipeline of actions. The major steps which constitute the process are depicted in Figure 3.1. An extensive and more complex description of each step is developed in the following sections.

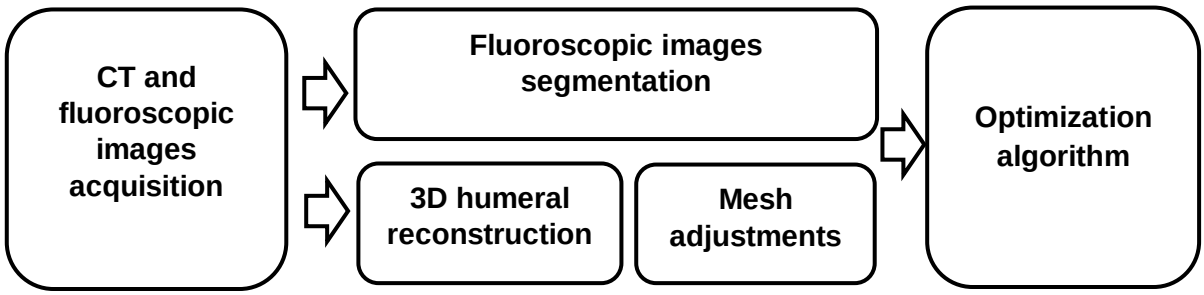

Figure 3.1 - Computational pipeline followed in this study

A brief description of the processes behind the acquisition of medical CT and fluoroscopic images from the subject used in this research are introduced. Then, the imaging techniques culminated in the final geometry of the 3D humerus model and segmentation of fluoroscopic images are presented. Finally, the automatic matching procedure is described. This study used CT and fluoroscopic images from a subject whose personal and medical information will remain undisclosed. These exams were performed at Hospital Santa Maria.

3.1 Image processing and final geometry

This section is divided into two subsections each dedicated to the final geometries obtained in this study: (1) the reconstruction of a 3D humerus model using CT images and (2) the segmentation of fluoroscopic images to obtain humerus contours.

3.1.1. 3D model reconstruction

ITK-SNAP is an open-source software application used to segment structures of 3D medical images. This software provides a semi-automatic segmentation through the application of active contour methods, as well as the possibility to navigate through three-dimensional medical images and delineate anatomical regions of interest.

To create a 3D humeral model, the subject's right shoulder was CT imaged. With ITK-SNAP 3D humerus model using the CT images is possible to be created. This process started with the adjustment of the image contrast and the selection of the region of interest (ROI) that accentuates the borders and focus the area of the humerus.

Next the thresholding parameters were set. A range of intensities of the image were classified into background and foreground. This is the process of thresholding the image to obtain the so-called feature image. The foreground intensities are assigned to a value of 1 while the background intensities are assigned to a value of -1. A value of 0 is assigned to intensities that are on the borderline between the background and foreground. The goal is to make sure that the voxels inside the humeral bone tissue are assigned positive values by adjusting the thresholding parameters. Next the user positions several bubbles on the image which evolve to take the shape of the humerus, as represented in Figure 3.3. The evolution of the bubbles is dependent on the image intensities defined in the feature image.

Figure 3.2 Thresholding evolution on ITK-SNAP for several iterations

Some imperfections derived from the presence of noise and partial volume effect were corrected by performing manual segmentation.

The surface mesh of the humerus created with ITK-Snap was exported to MeshLab. MeshLab is an open source software for processing and editing 3D triangular meshes. In order to smooth staircase artefacts derived from CT scanning, the 3D humerus model undergone a filtering correction. A Laplacian Smooth filter was applied to the whole geometry of the humerus. The final geometry of the 3D humerus model is represented in Figure 3.3

Next, the 3D surface mesh of the humerus was imported to Matlab© software as a 3D point cloud. The original point cloud was downsampled to decrease computation time.

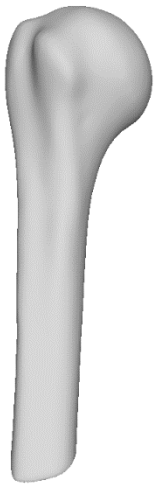

Figure 3.3 – Final geometry of the 3D humerus model after a filter correction in Meshlab

3.1.2 – Fluoroscopy images segmentation

Dual plane fluoroscopic imaging systems are technically challenging to implement in clinical environment [19, 2, 3, 29, 34], Two fluoroscopes must be synced to record images simultaneously, which requires various calibration tools and software development specific to the imaging system [35]. For this reason, these systems are not accessible in many medical institutions. In this study, only single plane fluoroscopy images were able to be obtained. During the exam, the subject was oriented so that all the right shoulder joint was covered. The subject was asked to move his arm through a series of abduction angles imaged by the fluoroscope. These images are stored electronically with an 8-bit grey scale and a resolution of 1024×1024 pixels.

The contours of the humerus from the fluoroscopic images were extracted by segmentation using the active contours method. Firstly, a ROI limiting the humerus areas was manually defined. This region minimizes the presence of the clavicle and the scapula that will not be segmented. Then, the contours were saved as a list of 2D spatial points. As observed in Figure 3.4, a perfect geometry of the humerus was not obtained. Given the overlap of the humerus with the scapula and the clavicle on the fluoroscopic image, the head of the humerus when segmented did not present a total rounded shape.

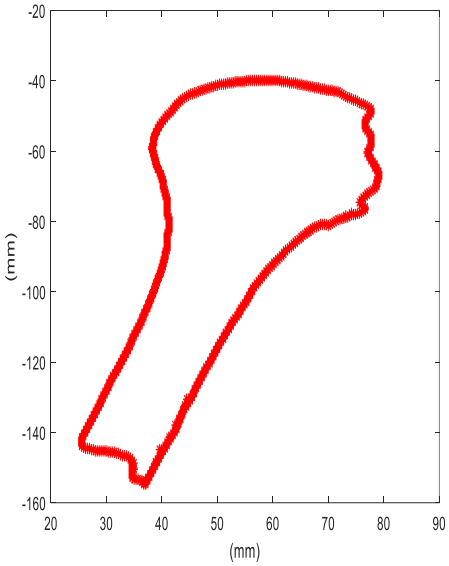

Figure 3.4 – Humerus contours after segmentation of the single-plane fluoroscopic image

3.2 – Optimized matching method

The matching process was formulated as an optimization procedure that minimizes the error between the projected 3D model and respective fluoroscopic image contours. More precisely, the aim was to determine the optimum 3D bone model pose which makes that the its projection matches the outlines captured from the fluoroscopic image taken as the reference. Note that the 3D model pose is defined in 6DOF: the three components of the position vector and the three Euler angles in relation to the global coordinate system. The objective function is a scalar function with six independent variables which define the 3D humerus model.

3.2.1 – Transformation of model points

In the global coordinate system, each point of the 3D model, noted as p_i, is transformed from an initial pose to a new position and orientation, noted as $\widetilde{p_i}$, by six independent variables. Each point undergoes a 3D translation described by the vector $\mathbf{T} = \{x, y, z\}^T$ and a 3D rotation described by the rotation matrix $\mathbf{R}$ in (2). The rotation matrix can be defined taking into consideration different rotation sequences. In this case, a $Y - Z - X$ Euler sequence using the angles α, β and γ was applied. The rotation in X corresponds to an α angle, a rotation in Y to a β angle and a rotation in Z to a γ angle.

$$\widetilde{p_i} = \mathrm{R}\,(p_i) + \mathrm{T} \tag{1}$$

$$\mathrm{R} = \begin{bmatrix} \cos\beta\cos\gamma & -\sin\gamma & \sin\beta\cos\gamma \\ \cos\alpha\cos\beta\sin\gamma + \sin\alpha\sin\beta & \cos\alpha\cos\gamma & \cos\alpha\sin\beta\sin\gamma - \sin\alpha\cos\beta \\ \sin\alpha\cos\beta\sin\gamma - \cos\alpha\cos\beta & \sin\alpha\cos\gamma & \sin\alpha\sin\beta\,sin\gamma + \cos\alpha\cos\beta \end{bmatrix} \tag{2}$$

As soon as the 3D model is transformed to a new pose, the ith point $\widetilde{p_i}$, of the 3D model is projected. Depending on the type of fluoroscopic images used, single or dual fluoroscopic images, the 3D humeral model is projected onto one or two planes respectively. Then the boundary points of the resulting 2D model are extracted using a function implemented in Matlab©.

3.2.2 - Objective functions for optimization

To make the projected 3D humerus model match the fluoroscopic outline, different features can be evaluated. Three objective functions were thus tested: the minimization of the moments of inertia, the intersection area and the distance between the projected and fluoroscopic contour points. These three objective functions are described with more detail next.

3.2.2.1 – Objective function: Moments of Inertia

The optimization was defined in this case as the minimization of the difference between the two eigenvalues of the fluoroscopic model ($\lambda_{Ref\,1}$and $\lambda_{Ref\,2}$) and the projected 3D model (λ_1 and λ_2). This operation is expressed in equation (3). Also, the eigenvectors of the projected 3D model (υ) along one direction were ensured to be orthogonal to the eigenvectors of the fluoroscopic model (v_{Ref}) along the contrary direction, i.e. their dot product was zero. This operation is expressed in equation (4) and is represented in Figure 3.5. The objective function J is a combination of these two operations and is formulated by the equation (5) for each projection plane k. Note that through these operations, only the rotation components of the 3D model are optimized. To optimize the respective translation components, the distance between the centroids of the two models would have to be minimized.

$$\lambda_T = \sum_{k=1}^{2} \left(\frac{\lambda_{1,k}}{\lambda_{Ref\,1,k}} - 1\right)^2 + \left(\frac{\lambda_{2,k}}{\lambda_{Ref\,2,k}} - 1\right)^2 \quad (3)$$

$$v_T = \sum_{k=1}^{2} \left(v_{Ref\,1,k} \cdot \upsilon_{2,k}\right)^2 + \left(v_{Ref\,2,k} \cdot \upsilon_{1,k}\right)^2 \quad (4)$$

$$J = v_T + \lambda_T \quad (5)$$

The eigenvalue component λ_T in equation (3) reached much higher values than the eigenvector component v_T . To make the two terms have the same influence on the equation, the eigenvalue component λ_T was normalized.

The eigenvectors and eigenvalues of the two models were obtained by calculating the tensor of inertia I associated to each model. The tensor of inertia I assumes the form of a 2D matrix, as expressed in (6).

$$[I] = \begin{bmatrix} Ixx & Ixy \\ Iyx & Iyy \end{bmatrix} \quad (6)$$

.

$$I_{xx} = \sum_{i=1}^{q_k} m_i y_i^2 \quad (7)$$

$$I_{yy} = \sum_{i=1}^{q_k} m_i x_i^2 \quad (8)$$

$$I_{xy} = I_{yx} = -\sum_{i=1}^{q_k} m_i\, x_i y_i \qquad (9)$$

Ixx and Iyy are the moments of inertia of the two models with respect to the X and Y axes respectively. The moments of inertia of each model were calculated by summing their outlines points i by their distance squared from the axes, as defined in (7) and (8). m_k is the mass of each outline point which was considered as 1. The quantities I_{xy}, and I_{yx} are the products of inertia formulated in (9).

For a 2D body, the principal axes of inertia are two orthogonal axes (an XY coordinate system), for which the products of inertia are zero, and the inertia matrix takes a diagonal form [36]. The eigenvectors of I represent the principal axes of the model. In terms of physical meaning, the eigenvectors are the directions about which the object's resistances to rotation is distributed evenly [37]. The eigenvalues are related to the magnitude of the eigenvector.

An illustration of this optimization process is represented in Figure 3.7. The direction of the two orthogonal axes is given by the eigenvectors and its magnitude is given by the eigenvalues. Since the translation components were not optimized, the two models were superimposed. The origin of the orthogonal axes represents the centroid of the two models. When the orthogonal axes of the two models coincide, the two models are perfectly aligned and superimposed.

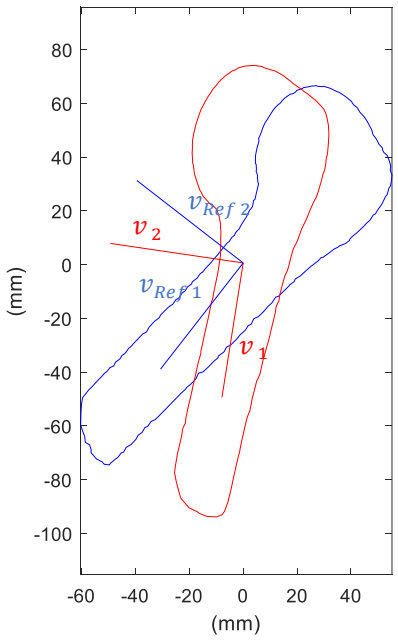

Figure 3.5 – Representation of one iteration of the optimization process between the eigenvectors of the projected 3D humerus model in red (v) and the humerus model obtained from the fluoroscopic images in blue (v_{Ref}). The objective is to make that these orthogonal axes coincide.

3.2.2.2 – Objective function: Areas

The outline points of the projected 3D model and the segmented fluoroscopic image define a 2D polygon. In application of single or dual projection planes k, I_k represents the intersection area between the two polygons and Ref_k the area of the polygon defined by the outlines of segmented fluoroscopic image. The objective function used in this case is formulated in (10) and minimizes the difference between I_k and Ref_k. When this difference is equal to zero, the two polygons are completely intersected. An illustration of one iteration of this optimization process is represented in Figure 3.5.

$$J = \sum_{k=1}^{2} (I_k - Ref_k)^2 \tag{10}$$

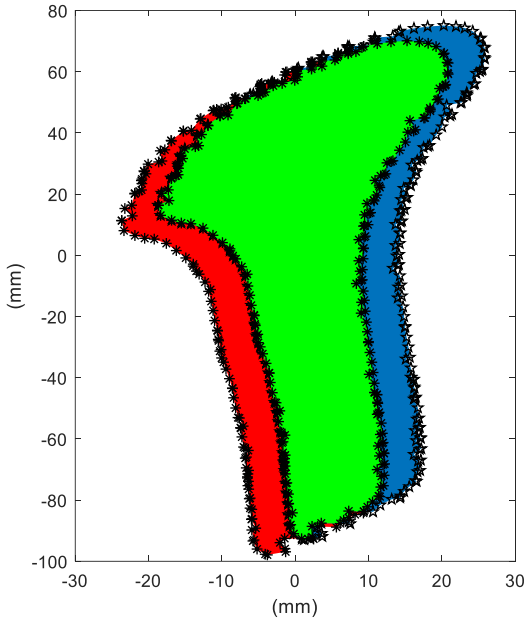

Figure 3.6. – An iteration of the projected 3D model in red, taken as the reference polygon, and the fluoroscopic model in blue. The green region represents the intersection area of the two models. When the green area equals the blue region the two polygons are totally overlapped.

3.2.2.3 – Objective function: distances

For each outline point of the projected 3D model $\widetilde{P_{k,i}}$, the closest point from the fluoroscopic outlines was selected g_k. The distance $d_{k,i}$ between two closest points was calculated using a function already implemented in Matlab®. For each projection plane k, the distances are summed and divided by the total number of points q_k. The resulting normalized distance is returned as the value of the objective function J formulated in (11). The optimization process is thus expressed as the minimization of the distances between the outline points of the projected 3D model and the points of the segmented fluoroscopic image. An illustration of one iteration of this optimization process is represented in Figure 3.6.

$$J = \sum_{k=1}^{2} \frac{1}{q_k} \sum_{i=1}^{q_k} {d_{k,i}}^2 = \sum_{k=1}^{2} \frac{1}{q_k} \sum_{i=1}^{q_k} (g_k - \widetilde{P_{k,i}})^2 \qquad (11)$$

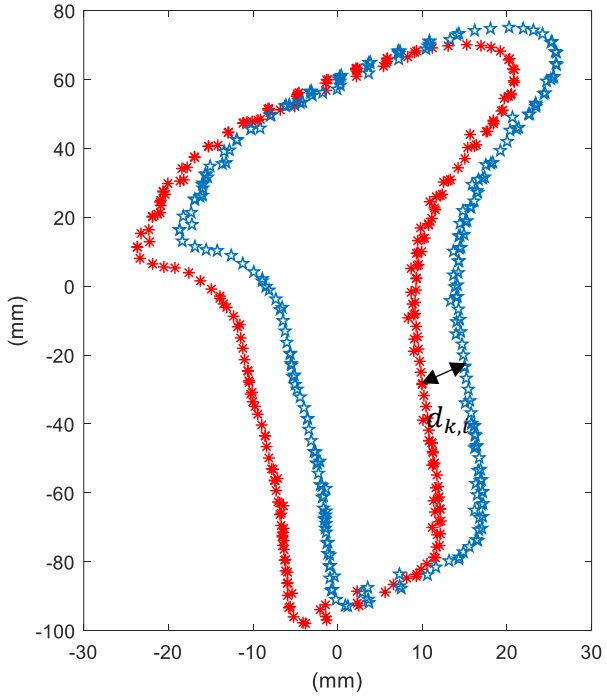

Figure 3.7 An iteration of the minimization of the distances between the outline points of the projected 3D model in red and the segmented fluoroscopic image in blue taken as the reference. $d_{k,i}$ represents the distance to be optimized between two closest outline points of the models.

3.3 – Validation

The minimization of the three objective functions was accomplished with a gradient-free based algorithm - the genetic algorithm. This algorithm is implemented on the Matlab© software. The minimization routine is said to converge if the average relative change in the value of the objective function over the iterations is less than or equal to 10^{-4} or when the number of iterations exceeds 200**.** Regarding the parameters used with the GA, a population size of 400 was set for all the tests. Also, so that the optimization process can start, it was used the default function implemented in Matlab© which creates an initial population which satisfies the constrains applied. The optimization process was accelerated by using parallel computing. This feature was activated in Matlab© software to stablish a parallel pool of four workers.

To validate the accuracy of the method in reproducing the 6DOF spatial positions of the humerus, the algorithm was tested in an idealized and in vivo environment. An idealized testing environment was created to isolate systematic errors and bias related to the geometry of the humerus and extraction of contours from the fluoroscopic images [35]. This test is extremely important to evaluate the accuracy of the optimization algorithm. To assess the performance of the algorithm when running real data, an *in vivo* test was performed. This test consists on using *in vivo* fluoroscopic images from one living subject. With this test, only a qualitative analysis of 00the results was achieved.

3.3.1 - Idealized Environment Test

The purpose of using an idealized environment test was to determine the optimized matching algorithm's accuracy in determining humerus poses in 6DOF under controlled conditions.

Defining five different poses of the 3D model, five idealized fluoroscopic images were created by projecting the 3D model onto one and two plans. Using these poses as reference, the optimization process aimed to find the positions and orientations which were known *a priori.* The error of the optimized matching process is measured by comparing the optimized pose with the reference pose.

Given the impossibility of obtaining *in vivo* dual fluoroscopic images, these images were created in an idealized environment. Idealized dual fluoroscopic images were obtained by projecting the 3D model onto the XZ and YZ plan. Idealized single fluoroscopic images were also obtained by projecting the 3D humerus model onto the XZ plan.

To analyze the sensitivity of the algorithm to position and orientation**,** two kind of poses were tested: three poses with only one rotation about one axis (SP) and two poses with rotations and translations about the three axes randomly generated using a Gaussian distribution (RGP). These poses are listed in Table 3.1.

Table 3.1 – Orientation and position of the five idealized humerus poses

	Rotation			Translation		
	$\boldsymbol{\alpha}$ (°)	$\boldsymbol{\beta}$ (°)	$\boldsymbol{\gamma}$ (°)	$\boldsymbol{x}$ $(\boldsymbol{mm})$	$\boldsymbol{y}$ $(\boldsymbol{mm})$	$\boldsymbol{z}$ $(\boldsymbol{mm})$
SP1	0	0	0	0	0	0
SP2	60	0	0	0	0	0
SP3	30	0	0	0	0	0
RGP1	100.04	-38.56	-110.58	7.90	-11.61	12.41
RGP2	-93.51	54.20	-98.49	14.73	8.70	17.32

With the objective of finding the best optimized solutions, three objective function were tested under idealized environment: the minimization of the areas, distances and moments of inertia. The sensitivity of the algorithm was tested by constraining the search space of the optimizer to a specific range from the ideal poses. In optimization problems, the search space is the set of all possible solutions (variable values) that satisfies the constraints. A range of $\pm 5\ mm$ in translation and $\pm 5\,°$ in rotation and a range of $\pm 20\ mm$ in translation and $\pm 20\,°$ in rotation from the ideal pose were tested.

Given the strong randomness component of GA, the algorithm is run multiple times to eliminate any possible random bias. This optimization procedure was performed 20 times for each humerus pose. The error was measured from the optimized pose to the reference pose.

3.3.2 – *In vivo* test

This test employed *in vivo* single fluoroscopic images of the humerus of one living subject taken with the fluoroscopic system. Only one fluoroscopic image of the humerus was selected to test the automatic matching algorithm. The segmented fluoroscopic images are now the gold standard pose that the projected 3D model needs to match. The selected pose was submitted to 20 independent optimizations. The objective function used was the minimization of the distances.

As the X-ray beam diverges from the X-ray source, the image produced on the fluoroscopic film is always slightly larger than the original object [45]. This is the so called magnification effect. With the magnification factor, the size of the object with the right proportion in relation to its actual size is possible to obtained [38]. In this case, given the experimental conditions under which the fluoroscopy exam was performed, the magnification factor was not able to be calculated. To overcome this limitation, it was made an approximation of its value by performing several tests until the projected 3D humerus model and the fluoroscopic contours have similar sizes. The magnification factor used was 0.35.

The accuracy of the automatic 2D-3D matching algorithm in this test was not quantified as no gold standard was present to know the actual spatial position and orientation of the humerus. Only a qualitative analysis of the results was performed by graphically evaluating if the two matching models were satisfactory overlapped and aligned.

Given some limitations associated to this test, as segmentation errors and the inexistence of the exact magnification factor, the final positions and orientations of the humerus resulted from the first optimization were submitted to a second optimization process. To achieve better results, the search space and convergence criteria were extended. The search space was constrained to a range of $\pm 30\ mm$ in translation and $\pm 30\ °$ in rotation from the final positions and orientations obtained from the first optimization. The convergence criteria was extended to a maximum number of generations of 500 and a function tolerance of 10^{-6}.

3.4 – Analysis of the results

A quantitative analysis of the results was only performed on the idealized environments test. For each objective function tested, the mean absolute error associated to each pose was determined. For 20 optimizations ($N = 20$), the error $\Delta\varepsilon$ is formulated in (12) and was calculated for each pose variable. ε_{ref} represents the variable value of the reference pose and ε the variable value optimized.

$$\Delta\varepsilon = \frac{\sum_{i=1}^{N} \left|\varepsilon_{ref} - \varepsilon\right|}{N} \tag{12}$$

The standard deviation associated to each pose was also calculated.

With idealized single fluoroscopic images, the error was reported as in-plane ($\Delta\beta$ Δx Δz) and out-plane ($\Delta\alpha$ $\Delta\gamma$ Δy).

The analysis of the results considered the total of 20 optimizations. In some cases, to better analyze the accuracy of each objective function, the three optimizations with the lowest objective function value were also considered. For these cases both the mean average error as the standard deviation were calculated.

Chapter 4

Results

In this chapter, the results obtained with the developed method in determining humerus poses in 6DOF are presented. This chapter is divided into two sections. Section (1) consists on a quantitative analysis of the accuracy of the method under an idealized testing environment using different objective functions. Section (2) reports a qualitative analysis of the accuracy of the method with an *in vivo* environment test.

4.1 Idealized environment test

This test evaluated the accuracy of the method in determining known humerus poses using idealized dual and single fluoroscopic images. Three objective functions were tested: minimization of the moments of inertia, area and the distances between the outlines of the projected 3D model and the segmented fluoroscopic images. The twenty optimizations obtained for each pose are listed in Appendix

4.1.2 Comparison between objective functions

This subsection presents the results obtained with each objective function tested under the same conditions: for when the search space of the optimizer was constrained to a range of $[\pm 5\,mm;\ \pm 5\,°]$ and $[\pm 20\,mm;\ \pm 20\,°]$ from the ideal pose. These tests used idealized dual fluoroscopic images and considered poses with one rotation about one axis (SP) and poses with translations and rotations randomly generated about the three axes (RGP). The twenty optimizations obtained for each pose under the two ranges are listed in Appendix A and B.

4.1.2.1 Range of $\pm\ 5\ mm$ in translation and $\pm 5\ °$ in rotation

The errors associated to the five poses using the minimization of the distances, area and moments of inertia are listed in Table 4.1 considering the total of 20 optimizations. For the minimization of the areas and moments of inertia, the error of the three best optimizations associated to each pose is listed in Table 4.2.

For the minimization of the distances, the three SP recorded a maximum error of $0.04\ \pm 0.03°$ in rotation and $0.00\ \pm 0.00\,°\,mm$ in translation. In turn, the two RGP were reproduced with a maximum error of $0.64\ \pm\ 0.48°$ in rotation and $0.00\ \pm 0.00\,°\,mm$ in translation.

For the minimization of the areas, the errors in rotation and translation were higher than those obtained with the minimization of the distances. Regarding the three SP, higher errors in γ than in β and α were observed. For these poses, the maximum error in γ reached $2.80\ \pm 1{,}09°$ and $0.52\ \pm 0.23\,°$ for the other two angles. In relation to the translation components, the three SP recorded a maximum error of $0{,}19\ \pm 0{,}43\,mm$. For RGP, this pattern was not so obviously observed - for each RGP, the maximum error in rotation occurred in different variables. Moreover,

some discrepancies were observed between the two RGP – for example, RGP1 recorded much higher errors than RGP2. Considering the three best optimizations, lower errors in rotation and translation were found. The three SP recorded a maximum error in γ of 1.19 ± 1.00 ° and 0.11 ± 0.03 ° in the two other angles. The translation components recorded a maximum error of $0.69 \pm 0.96\, mm$. For the two RGP, a maximum error of 1.50 ± 0.69 ° in rotation and $0.55 \pm 0.66\, mm$ in translation was recorded.

For the minimization of the moments of inertia, since the translation variables were not optimized, only the errors in rotation are presented. In general, the errors obtained were higher than those obtained with the minimization of the distances. Likely, these errors were similar to those obtained with the minimization of the areas. The three SP also recorded higher errors in γ than in β and α. A maximum error in γ of $0{,}73 \pm 1{,}00$ ° and $0{,}73 \pm 0{,}43$ ° for the two other angles was recorded. For the two RGP, the maximum error reached $2{,}02 \pm 1{,}43$ °. When only the three best optimizations were considered, a slight decrease on the errors of SP and RGP was observed. A maximum error of 0.56 ° and 1.92 ° was recorded for SP and RGP respectively.

Table 4.1 - Mean absolute error associated to each pose for the minimization of the distances, areas and moments of inertia using idealized dual fluoroscopic outlines and a search space of $[\pm 5\,mm;\ \pm 5\,°]$ from the ideal poses.

	Model Pose	Rotation (°)			Translation (mm)		
		$\Delta\,\alpha$	$\Delta\,\beta$	$\Delta\,\gamma$	Δx	$\Delta\,\mathrm{y}$	$\Delta\,\mathrm{z}$
Distances	**RGP1**	0,13 ± 0,13	0,11 ± 0,11	0,05 ± 0,05	0,00 ± 0,00	0,00 ± 0,00	0,00 ± 0,00
	RGP2	0,63 ± 0,48	0,64 ± 0,48	0,07 ± 0,05	0,00 ± 0,00	0,00 ± 0,00	0,00 ± 0,00
	SP1	0,01 ± 0,01	0,02 ± 0,03	0,04 ± 0,03	0,00 ± 0,00	0,00 ± 0,00	0,00 ± 0,00
	SP2	0,01 ± 0,01	0,01 ± 0,01	0,02 ± 0,02	0,00 ± 0,00	0,00 ± 0,00	0,00 ± 0,00
	SP3	0,00 ± 0,00	0,03 ± 0,05	0,02 ± 0,04	0.00 ± 0,01	0,00 ± 0,00	0,00 ± 0,00
Areas	**RGP1**	2.99 ±1.38	1.62 ±0.73	1.55 ± 0.74	0.31 ± 0.22	0.85 ± 0.77	0.43 ± 0.31
	RGP2	0.88 ± 0.80	0.90 ±0.82	0.09 ± 0.09	0.00 ± 0.00	0.00 ± 0.00	0.00 ± 0.00
	SP1	0.02 ± 0.02	0.19 ±0.24	0.87 ± 1.12	0.07 ± 0.11	0.01 ± 0.01	0.02 ± 0.03
	SP2	0.07 ± 0.04	0.24 ±0.13	1.43 ± 0.79	0.01 ± 0.01	0.00 ± 0.00	0.01 ± 0.01
	SP3	0.15 ± 0.12	0.52 ±0.23	2.80 ± 1.09	0.05 ± 0.08	0.18 ± 0.19	0.19 ± 0.43
Moments of Inertia	**RGP1**	0.67 ± 0.55	0.89 ± 0.47	0.89 ± 0.62			
	RGP2	2.02 ± 1.43	1.80 ± 1.21	0.41 ± 0.23			
	SP1	0.43 ± 0.37	0.31 ± 0.25	0.73 ± 1.00			
	SP2	0.17 ± 0.17	0.38 ± 0.27	0.65 ± 0.68			
	SP3	0.20 ± 0.21	0.29 ± 0.21	0.42 ± 0.52			

Table 4.2 - Mean absolute error associated to the three best optimizations of each pose for the minimization of the areas and moments of inertia using idealized dual fluoroscopic outlines and a search space of $[\pm 5\,mm;\ \pm 5\,°]$ from the ideal poses.

	Model Pose	Rotation (°)			Translation (mm)		
		$\Delta\,\alpha$	$\Delta\,\beta$	$\Delta\,\gamma$	Δx	$\Delta\,\mathrm{y}$	$\Delta\,\mathrm{z}$
Areas	**RGP1**	1.5 ± 0.69	0.88 ± 0.28	0.74 ± 0.36	0.11 ± 0.07	0.55 ± 0.66	0.15 ± 0.08
	RGP2	0.14 ± 0.06	0.14 ± 0.06	0.01 ± 0.01	0.00 ± 0.00	0.00 ± 0.00	0.00 ± 0.00
	SP1	0.00 ± 0.00	0.01 ± 0.00	0.02 ± 0.01	0.00 ± 0.00	0.00 ± 0.00	0.00 ± 0.00
	SP2	0.01 ±0.00	0.03 ± 0.02	0.13 ± 0.08	0.00 ± 0.00	0.00 ± 0.00	0.00 ± 0.00
	SP3	0.10 ± 0.03	0.11 ± 0.03	1.19 ± 1.00	0.12 ± 0.16	0.23 ± 0.3	0.69 ± 0.96
Moments of Inertia	**RGP1**	0.43 ± 0.33	0.55 ± 0.27	0.64 ± 0.38			
	RGP2	1.92 ± 1.86	1.71 ± 1.00	0.28 ± 0.16			
	SP1	0.31 ± 0.19	0.10 ± 0.04	0.49 ± 0.33			
	SP2	0.14 ± 0.08	0.33 ± 0.19	0.28 ± 0.10			
	SP3	0.18 ± 0.20	0.11 ± 0.07	0.56 ± 0.66			

4.1.2.2 Range of $\pm 20\ mm$ in translation and $\pm 20\ °$ in rotation

For the range of $[\pm 20\ mm;\ \pm 20\ °]$, the errors associated to the five poses using the minimization of the distances, area and moments of inertia are listed in Table 4.3 considering the total of 20 optimizations. The error of the three best optimizations when using minimization of the areas and moments of inertia are listed in Table 4.2.

For the minimization of the distances, SP were reproduced with the same errors in rotation and translation than those obtained with the range of $[\pm 5\ mm;\ \pm 5\ °]$. The RGP were reproduced with an error of $0.00\ mm$ in translation and a maximum error of $1.39\ °$ in rotation, a value slightly higher than that obtained with the range of $[\pm 5\ mm;\ \pm 5\ °]$.

With the minimization of the intersection areas and the moments of inertia, both RGP and SP recorded higher errors in translation and rotation than those obtained with the previous range. Likely, the SP continued to record higher errors in γ than in α and β. This behavior was not so obviously detected with the RGP, as happened with the previous range.

For the minimization of the areas, when the three best optimizations were considered, the maximum errors were lower than those obtained with the 20 optimizations, but still high. SP were reproduced with a maximum error of $9.18 \pm 0.08°$ in rotation and $0.81 \pm 1.02\ mm$ in translation. RGP were reproduced with a maximum error of $5{,}64 \pm 0.85\ °$ in rotation and $0.73 \pm 0.31\ mm$ in translation.

For the minimization of the moments of inertia, considering the three best optimizations, the values were still high. SP were reproduced with a maximum error of $7.17 \pm 4.55\ °$ in γ and $1.73 \pm 1.38\ °$ on the two other angles. RGP were reproduced with a maximum error of $3.98 \pm 2.84°$.

Since the error values obtained under this range were high, even when only the three best optimizations were considered, a graphical analysis of the impact of these errors was performed. For each objective function, Figures 4.1 to 4.5 represent the best optimization for each pose. With the minimization of the distances, the five poses are perfectly aligned and overlapped. With the minimization of the areas and the moments of inertia, an insignificant variation on the matching of the two models is observed. Even for the RGP, which recorded higher errors, this variation is minimal.

Table 4.3 - Mean absolute error associated to each pose for the minimization of the distances, areas and moments of inertia using idealized dual fluoroscopic outlines and a search space of $[\pm 20\ mm;\ \pm 20\ °]$ from the ideal poses.

	Model Pose	Rotation (°)			Translation (mm)		
		$\Delta\alpha$	$\Delta\beta$	$\Delta\gamma$	Δx	Δy	Δz
Distances	**RGP1**	0,17 ± 0,21	0,15 ± 0,2	0,06 ± 0,08	0,00 ± 0,00	0,00 ± 0,00	0,01 ± 0,01
	RGP2	1,37 ± 1,29	1,39 ± 1,31	0,14 ± 0,11	0,00 ± 0,01	0,00 ± 0,01	0,00 ± 0,00
	SP1	0,01 ± 0,01	0,01 ± 0,01	0,02 ± 0,02	0,00 ± 0,00	0,00 ± 0,00	0,00 ± 0,00
	SP2	0,01 ± 0,01	0,01 ± 0,01	0,01 ± 0,02	0,00 ± 0,00	0,00 ± 0,00	0,00 ± 0,00
	SP3	0,01 ± 0,01	0,06 ± 0,1	0,05 ± 0,08	0,01 ± 0,02	0,00 ± 0,00	0,00 ± 0,00
Areas	**RGP1**	9.77 ± 2.97	6.43 ±2.97	5.66 ± 2.10	0.57 ± 0.36	0.78 ± 0.62	0.76 ± 0.59
	RGP2	1.12 ± 0.96	1.15 ±0.99	0.12 ± 0.10	0.00 ± 0.00	0.00 ± 0.01	0.00 ± 0.01
	SP1	0.03 ± 0.03	0.57 ±0.46	2.18 ± 1.81	0.12 ± 0.10	0.03 ± 0.03	0.02 ± 0.03
	SP2	0.60 ± 0.06	1.77 ±0.24	10.14 ± 0.92	0.08 ± 0.05	0.07 ± 0.01	0.08 ± 0.01
	SP3	0.46 ± 0.43	2.30 ±1.40	11.17 ± 5.86	0.29 ± 0.24	0.39 ± 0.46	0.36 ± 0.52
Moments of Inertia	**RGP1**	4,57 ±4,36	4,86 ±5,09	2,86 ±3,77			
	RGP2	6,61 ± 4,38	9,86 ± 4,21	2,26 ± 1,29			
	SP1	1,43 ± 0,88	1,67 ± 1,1	4,23 ± 5,48			
	SP2	1,39 ± 0,98	1,16 ± 0,88	6,82 ± 4,66			
	SP3	0,79 ± 0,55	0,80 ± 0,50	1,41 ± 1,50			

Table 4.4 - Mean absolute error associated to the three best optimizations of each pose for the minimization of the areas and moments of inertia using idealized dual fluoroscopic outlines and a search space of $[\pm 20\ mm;\ \pm 20\ °]$ from the ideal poses.

	Model Pose	Rotation (°)			Translation (mm)		
		$\Delta\alpha$	$\Delta\beta$	$\Delta\gamma$	Δx	Δy	Δz
Areas	**RGP1**	5.64 ± 0.85	3.05 ± 0.59	2.96 ± 0.52	0.40 ± 0.10	0.73 ± 0.31	0.51 ± 0.22
	RGP2	0.12 ± 0.07	0.13 ± 0.07	0.01 ± 0.01	0.00 ± 0.00	0.00 ± 0.00	0.00 ± 0.00
	SP1	0.01 ± 0.00	0.01 ± 0.00	0.03 ± 0.01	0.00 ± 0.00	0.00 ± 0.00	0.00 ± 0.00
	SP2	0.57 ± 0.04	1.43 ± 0.05	9.18 ± 0.08	0.13 ± 0.04	0.06 ± 0.00	0.09 ± 0
	SP3	0.08 ± 0.05	0.49 ± 0.26	3.43 ± 0.43	0.06 ± 0.05	0.29 ± 0.34	0.81 ± 1.02
Moments of Inertia	**RGP1**	1.31 ± 1.21	1.36 ± 0.45	1.31 ± 0.92			
	RGP2	3.98 ± 2.84	3.59 ± 1.74	0.36 ± 0,15			
	SP1	0.91 ± 0.69	1.73 ± 1.39	3.17 ± 2.25			
	SP2	0.64 ± 0.23	1.16 ± 0.79	7.17 ± 4.56			
	SP3	0.17 ± 0.06	0.24 ± 0.13	0.23 ± 0.25			

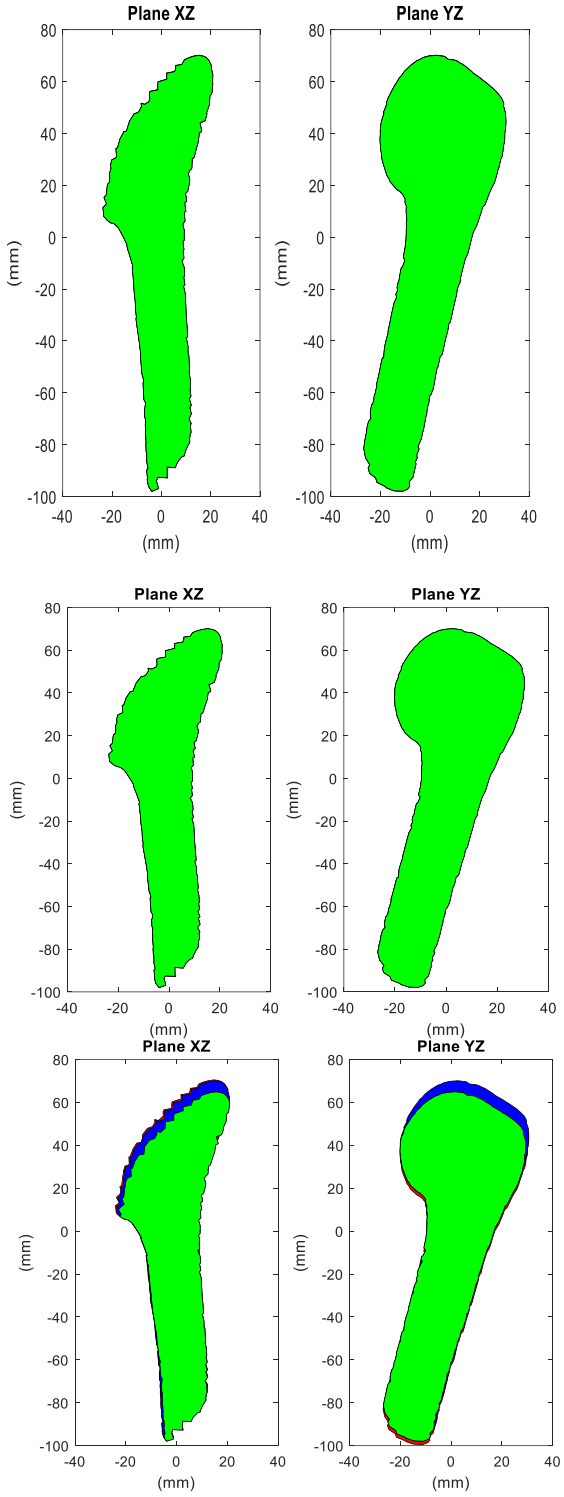

Figure 4.1 – Best solution obtained for SP1 when minimizing the distances (a), the areas (b) and the moments of inertia (c). The humeri represented in red and blue denote the optimized pose and the reference pose, respectively, while the green area represents the interaction between the two bones.

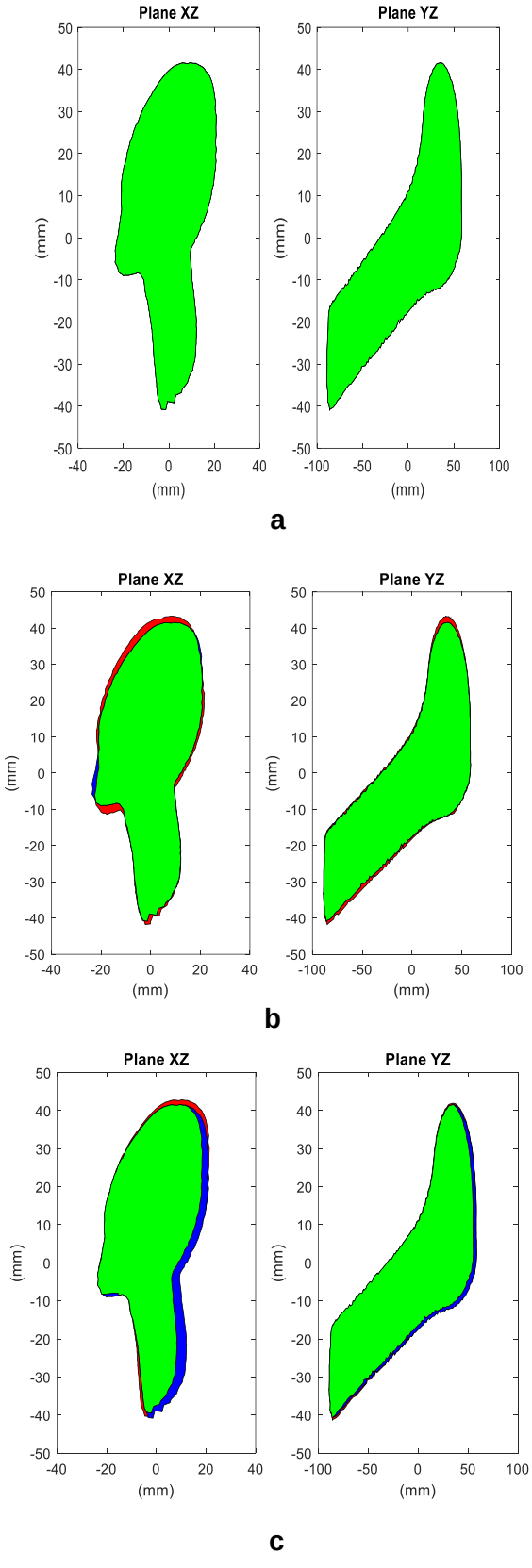

Figure 4.2 – Best solution obtained for SP2 when minimizing the distances (a), the areas (b) and the moments of inertia (c). The humeri represented in red and blue denote the optimized pose and the reference pose, respectively, while the green area represents the interaction between the two bones.

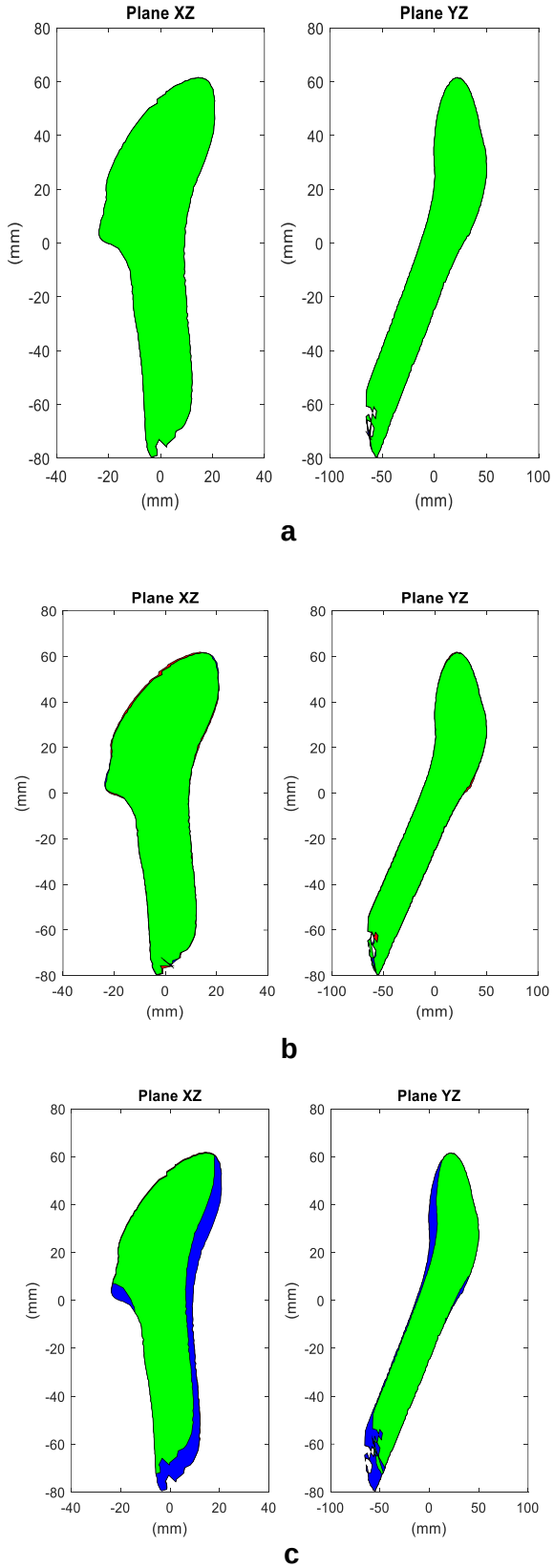

Figure 4.2 – Best solution obtained for SP3 when minimizing the distances (a), the areas (b) and the moments of inertia (c). The humeri represented in red and blue denote the optimized pose and the reference pose, respectively, while the green area represents the interaction between the two bones.

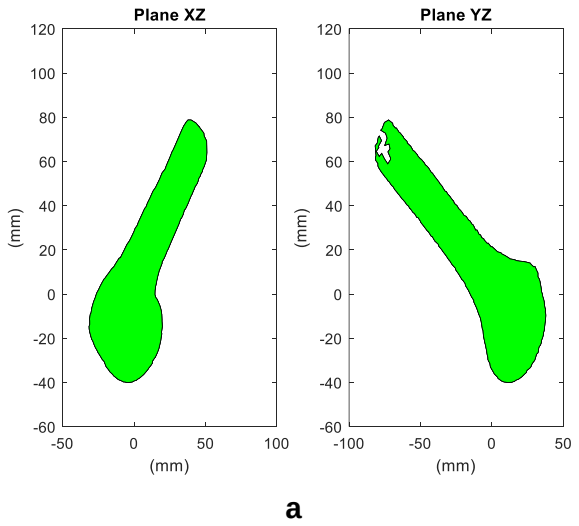

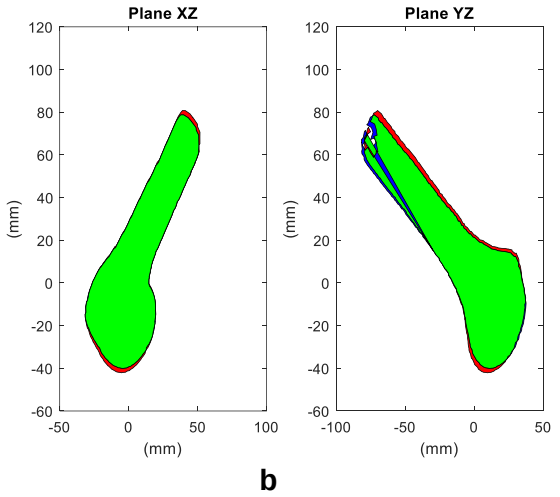

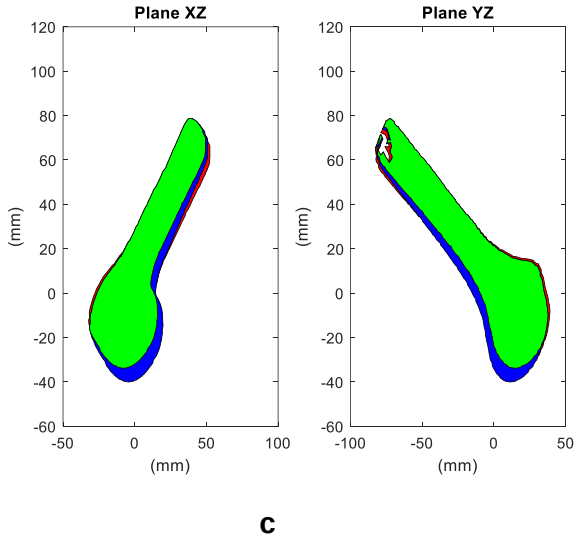

Figure 4.3 – Best solution obtained for RGP1 when minimizing the distances (a), the areas (b) and the moments of inertia (c). The humeri represented in red and blue denote the optimized pose and the reference pose, respectively, while the green area represents the interaction between the two bones.

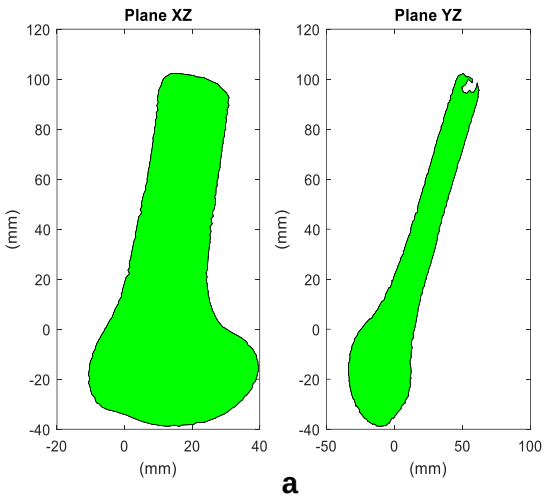

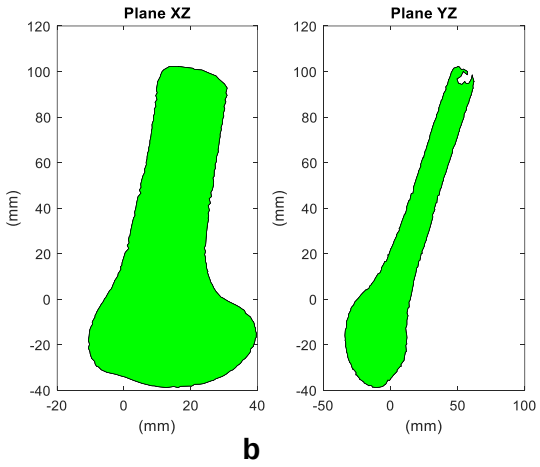

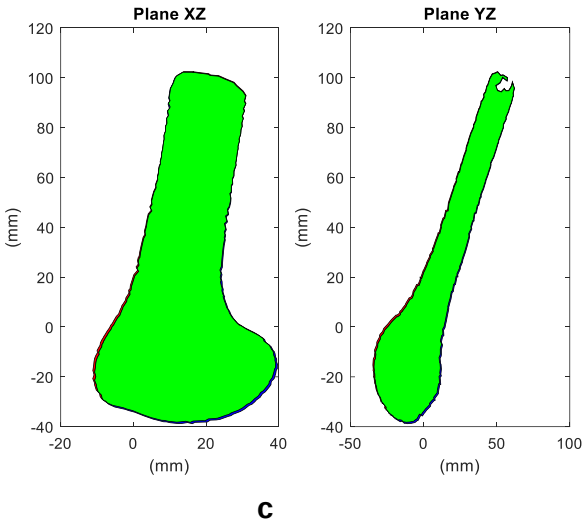

Figure 4.4 – Best solution obtained for RGP2 when minimizing the distances (a), the areas (b) and the moments of inertia (c). The humeri represented in red and blue denote the optimized pose and the reference pose, respectively, while the green area represents the interaction between the two bones.

4.1.3 Single plane optimization

Since the minimization of the distances was the objective function which yielded the most accurate results, single plane optimization was also tested with this function. The errors associated to the five poses using idealized single fluoroscopic outlines constraining the search space to a range of $[\pm 5\ mm;\ \pm 5\ °]$ and $[\pm 20\ mm;\ \pm 20\ °]$ from the ideal pose are listed in Table 4.5 and 4.6 respectively. The twenty optimizations obtained for each pose are listed in Appendix C.

For the range of $[\pm 5\ mm;\ \pm 5\ °]$, the three SP recorded a maximum in-plane error of $0{,}01 \pm 0{,}01°$ in rotation and $0{,}00\ mm$ in translation. Along the out-plane direction higher errors in translation were recorded, with a maximum of $2.53 \pm 1.34\ mm$. For the RGP, the in-plane error of $1.18\ °$ in rotation and $0{,}00\ mm$ in translation, with a maximum out-plane error of $0.96\ °$ in rotation and $2.84\ mm$ in translation was recorded.

For the range of $[\pm 20\ mm;\ \pm 20\ °]$, the same behavior was observed: low in-plane errors at the expense of large out-plane errors in translation. These values were specially elevated for RGP. RGP recorded a maximum in-plane error of $3.14\ °$ in rotation and $0{,}70\ mm$ in translation, with a maximum out-plane error of $2.73 \pm 2.71°$ in rotation and $10.73 \pm 5.79\ mm$ in translation.

Table 4.5 - Mean absolute error associated to each pose when using the minimization of the distances, single idealized fluoroscopic outlines and a range of $[\pm 5\ mm;\ \pm 5\ °]$ from the ideal poses. Values referent to a total of 20 optimizations.

Model Pose	Rotation (°)			Translation (mm)		
	$\Delta\alpha$	$\Delta\beta$	$\Delta\gamma$	Δx	Δ y	Δ z
RGP1	0.15 ± 0.13	0.15 ± 0.14	0.06 ± 0.05	0.00 ± 0.00	2.62 ± 1.53	0.01 ± 0.01
RGP2	0.96 ± 0.86	1.18 ± 0.9	0.1 ± 0.07	0.01 ± 0.00	2.84 ± 1.32	0.00 ± 0.00
SP1	0.02 ± 0.02	0.01 ± 0.01	0.03 ± 0.02	0.00 ± 0.00	2.32 ± 1.11	0.00 ± 0.00
SP2	0.00 ± 0.00	0.01 ± 0.01	0.01 ± 0.01	0.00 ± 0.00	2.53 ± 0.00	0.00 ± 0.00
SP3	0.01 ± 0	0.01 ± 0.01	0.03 ± 0.04	0.00 ± 0.00	2.52 ± 1.34	0.00 ± 0.00

Table 4.6 - Mean absolute error associated to each pose when using the minimization of the distances, single idealized fluoroscopic outlines and a range of $[\pm 20\ mm;\ \pm 20\ °]$ from the ideal poses. Values referent to a total of 20 optimizations.

Model Pose	Rotation (°)			Translation (mm)		
	$\Delta\alpha$	$\Delta\beta$	$\Delta\gamma$	Δx	Δ y	Δ z
RGP1	0.17 ± 0.21	3.14 ± 6.35	0.4 ± 0.96	0.5 ± 1.27	9.76 ± 5.32	0.70 ± 1.81
RGP2	1.37 ± 1.29	2.86 ± 2.88	0.22 ± 0.21	0.01 ± 0.02	10.73 ± 5.79	0.02 ± 0.03
SP1	0.01 ± 0.01	0.01 ± 0.02	0.04 ± 0.03	0.00 ± 0.00	10.32 ± 6.22	0.00 ± 0.00
SP2	0.01 ± 0.01	0.01 ± 0.00	0.01 ± 0.01	0.00 ± 0.00	11.42 ± 6.23	0.00 ± 0.00
SP3	0.01 ± 0.01	0.01 ± 0.03	0.03 ± 0.05	0.00 ± 0.00	12.81 ± 4.28	0.00 ± 0.00

4.2 *In vivo* environment test

The *in vivo* environment test is used to evaluate the accuracy of the method under real world conditions. Since the accurate spatial position and orientation of the humerus is unknown, only a qualitative analysis of the results can be performed.

In general, none of the 20 optimizations generated a satisfactory match between the projected 3D model and the fluoroscopic outlines. Figure 4.6 represents the best match after two successive optimizations. In the first optimization, a considerable part of the head and the body of the humerus does not overlap the model obtained from the segmented fluoroscopic images. Moreover, they are not aligned. After a second optimization process, a greater overlap of the projected 3D model over the model from the fluoroscopic image is observed, however, they are still not aligned.

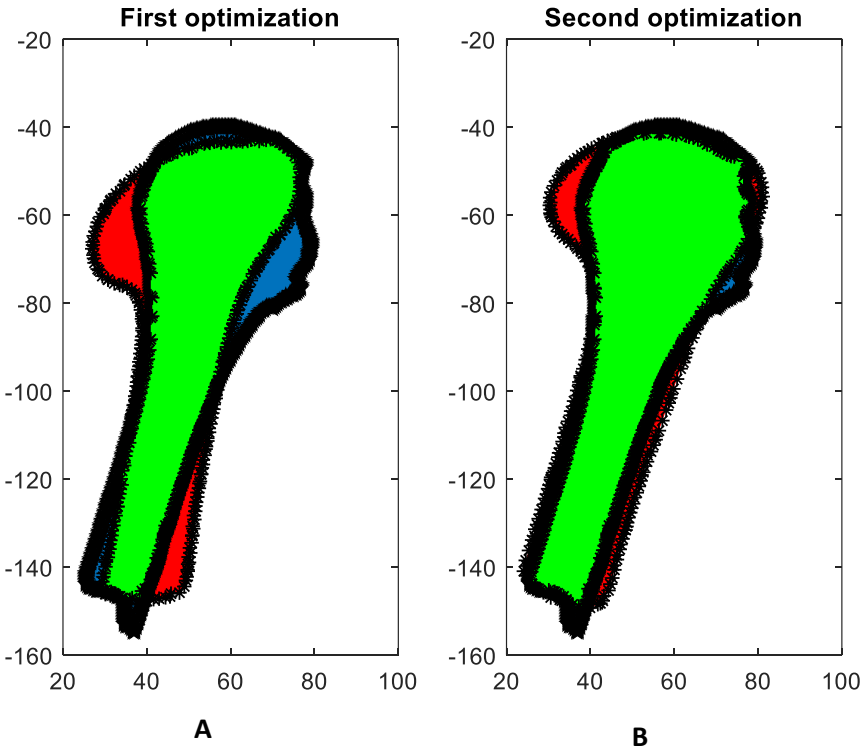

Figure 4.6 – Final match between the projected 3D humerus model (red) and the humerus outlines from the fluoroscopic images (blue) and respective intersection (green) after a first (A) and second (B) optimization process.

Chapter 5

Discussion

The shoulder is a complex system with high clinical relevance. Numerous techniques have been developed to accurately determine the shoulder kinematics. More recently, fluoroscopic image-model registration techniques have been explored due to its reported sub-millimeters levels of accuracy [35]. This technique reproduces the bone spatial positions through a 2D-3D image matching procedure that combines a 3D bone model with captured fluoroscopic images [35].

In this study, an automatic 2D-3D image matching method was developed to accurately reproduce humerus poses. An optimization algorithm was used to automatize the matching process, the genetic algorithm. The accuracy of the method was evaluated under an idealized environment. Idealized fluoroscopic images were created considering five poses of the 3D humerus model – three poses with only one rotation about one axis (SP) and two poses with rotations and translations about the three axes randomly generated (RGP). Using these models as reference, the optimization process aimed to find the rotations and translations known a priori. The search space of the optimizer was constrained to a range of ± 5 mm in translation and ± 5 ° in rotation and a range of ± 20 mm and ± 20 ° from the ideal pose. The search space represents the set of all possible solutions which satisfy these constraints. For each range, three objective functions were tested.

For the three objective functions tested, the data showed higher errors associated to RGP than to SP. As in RGP the rotations were randomly generated and about three axes, the search space of the optimizer was larger than in SP where only one rotation was applied, which may have contributed to this result.

The minimization of the distances was the objective function which showed more accuracy in reproducing both RGP and SP poses in space for both ranges. The errors for RGP were slightly higher than SP but still accurate. The results showed to be very consistent given the reduced standard deviation associated and the similar results obtained for both ranges. With dual fluoroscopic images and the range of $[\pm 5\,° ; \pm 5\,mm]$, SP recorded optimum error values of $0.02\,°$ $0.02\,mm$ in translation. The RGP recorded errors of $0.63\,°$ in rotation and $0.02\,mm$ in translation. For the range of $[\pm 20\,° ; \pm 20\,mm]$, SP recorded a maximum error of $0.05\,°$ in rotation and $0.02\,mm$ in translation. The RGP recorded a maximum error of $1.37\,°$ in rotation and $0.02\,mm$ in translation.

Higher error values were obtained when using the minimization of the moments of inertia and the intersection area with ideal dual fluoroscopic images. This result demonstrates that the algorithm used might have more sensitivity to optimize the distances than the areas and moments of inertia. With these two objective functions, the SP recorded higher errors in γ than in β and α. This result is likely due to the two projections have occurred in the plane XZ and YZ. These two planes are perpendicular to Y and X respectively, which allow a better approximation of the

correspondent angles, β and α. For a better approximation of γ, a projection in the perpendicular plane to the axis associated to $\boldsymbol{\gamma}$ would have to be made, i.e. in the XY plane. This behavior is not specially detected for RGP possibly due to the complexity of the rotations and translations associated. Considering only the three best optimizations, more accurate results were obtained, especially for the range $[\pm 5\,° ; \pm 5\,mm]$. For the range of $[\pm 20\,° ; \pm 20\,mm]$, both RGP and SP were still reproduced with high errors associated. These results suggest that these two objective functions have limited accuracy. Its performance is dependent on the size of the search space applied to the optimizer. Better results were attained with the range of $[\pm 5\,°;\ \pm\ 5\,mm]$ than with a range of $[\pm 20\,°;\ \pm\ 20\,mm]$ since when constraining the set of possible solutions to a narrower range, the optimizer is more likely to find an optimum solution.

The use of the minimization of the moments of inertia have limited applicability. Firstly, only the rotation components of the model can be optimized. Secondly, in case of the two models have different sizes, which may happen under an *in vivo* test, the principal axes of the models are also different which becomes difficult the alignment of the two models. Also, the use of the minimization of the areas cannot be generalized to all situations. In case the model from the fluoroscopic image is larger than the projected 3D model or vice-versa, the optimizer only ensures the two models are totally overlapped. The optimizer does not ensure the models are aligned. The minimization of the distances is the objective function which provides more robust results. By calculating the distance between the two models, a correspondence between the points is established, making that this function may be applied even in cases de two models have different sizes.

Given the accurate results obtained with the minimization of the distances, the matching process was also tested with idealized single fluoroscopic images. For the range of $[\pm 5\,° ; \pm 5\,mm]$, SP and RGP were accurately reproduced in the imaging plane (x, z, β), but at the expense of large errors along the out-plane direction. This behavior was also found with the range of $[\pm 20\,° ; \pm 20\,mm]$, but with higher errors associated. This test highlights the accuracy of dual plane optimization over single plane optimization. This is because out-of-plane errors of one projection are the in-plane errors of the other projection. Thus if in-plane motion is the primary measurement, this method can provide satisfactory accuracy using only single fluoroscopic images. If an analysis of the kinematics with 6DOF is the goal, dual plane optimization is necessary for sub-millimeter-degree resolution in all planes. .

In a general way, the results obtained compare positively to previous studies which also used an automatic 2D-3D image model technique for determining bone positions in 6DOF. In a study of shoulder kinematics, Z.Zhu et al. [35] determined humerus positions in space using a gradient-based algorithm to minimize the distances between the two matching models. This type of algorithms needs a humerus initial pose so that the optimization can start. For an idealized environment, the initial pose was randomly generated within the range of $\pm 5\,°$ in rotation and $\pm 5\,mm$ in translation from the ideal pose [35]. Maximum errors of $0{,}03\,mm$ in translation and $0{,}07\,°$ in rotation were found using dual fluoroscopic images [35]. For single fluoroscopic images, accurate results in in-plane motion were recorded at the expense of large out-plane errors. The

algorithm used in this study is not dependent on a single initial pose. GA starts with a set of initial poses (400) with the search space constrained to a specific range. Constraining the search space to $[\pm 5\,°; \pm 5\,mm]$ from the ideal pose, the minimization of the distances, and ideal dual fluoroscopic images, the results obtained with the presented method are consistent with those published, using both SP and RGP. For idealized single fluoroscopic images the same behavior of accurate in-plane results at the expense of large out-plane errors is observed for both RGP and SP. J. Bingham and G. Li [9] applied the same methodology as before to determine flexion positions of the tibia and femur using dual fluoroscopic images. This study used a range of $\pm 20\,°$ in rotation and $\pm 20\,mm$ to create the initial poses. Errors of $0{,}07\,mm$ in translation and $0{,}16\,°$ in rotation were recorded to determine femoral and tibial poses. In a study with single fluoroscopic images, Z. Zhu and G. Li [10] found that spatial poses of the femur and tibia can be determined with high accuracy in in-plane at the expense of large out-plane errors. Despite the different bone geometries, when a constraint range of $[\pm 20\,°; \pm 20\,mm]$ was used, the results from this study can be favorably compared to those from [9] and [10] if SP was used as reference. With RGP, the error values obtained with the presented method were higher.

In comparison with the previous studies, this study considered different objective functions, an analysis ignored in other studies. Also, the presented technique used genetic algorithms to perform the optimization process. This algorithm contributes to a more reliability of the results obtained. Due to its random nature, the genetic algorithm improves the chances of finding a global solution [44]. They do not depend on a single initial solution neither use the gradient information to find a solution, which decreases the risk of being trapped in a local minimum.

Since the actual position of the humerus in the fluoroscopic images is unknown, only a qualitative analysis of the accuracy of the method under *in vivo* conditions was performed. The optimization process in the *in vivo* test was accomplished through the minimization of the distances. The data showed that even after a second optimization of the results, the matching models were still not aligned. Two important factors may have contributed to the poor results. Firstly, the segmentation of the fluoroscopic images was susceptible to some errors, causing some geometric changes in the humerus natural morphology. Secondly, it was used an approximation of the magnification factor. This led to the use of fluoroscopic outlines with an inaccurate proportion, making the optimization process had occurred between models with different sizes.

The clavicle and the scapula present some characteristics that make them impossible to be accurately analyzed by the conventional methods. The scapula does not allow an accurate tracking through the use of surface markers because of its flat shape, soft tissue covering and significant subcutaneous motion [19]. Regarding the clavicle, only two bony landmarks are palpable, making that its axial rotation cannot be calculated through non-invasive techniques [20]. The presented method allows the kinematic analysis of any bony structure as long as the respective 3D model and fluoroscopic images are available. This technique can thus be a powerful tool to study the clavicle and the scapula kinematics. Moreover, this technique allows a

dynamic motion analysis, conversely to 3D static analysis usually applied. This optimized image matching method permit the processing of large quantities of image sets describing a dynamic motion. This is not so easily achieved if the matching process is performed in a manual way, as demonstrated in [3], where the 3D model is manually manipulated in space so that its projection match the fluoroscopy image.

The validation of the automatic matching algorithm to reproduce humerus positions in space has certain limitations. For the difficulty of establishing an *in vivo* gold standard pose of the humerus, only a qualitative analysis concerning the accuracy of the method under *in vivo* conditions was performed. For the same reason, the accuracy of the method was indirectly evaluated under idealized conditions which did not take into account possible effects of image segmentation.

In summary, this study presents an automatic 2D-3D image matching method to determine humerus poses in 6DOF using fluoroscopic images. The data showed that the optimization process, when using the minimization of the distances, provides accurate results using both single or dual fluoroscopic images. The minimization of the moments of inertia and intersection area are limited in their accuracy because of its dependence on the size of the search space applied to the optimizer. This method can be applied to any other bony structure as long as the respective fluoroscopic images and 3D model are available.

Chapter 6

Conclusions and Future Developments

The current work developed an automatic 2D-3D image matching method to determine humerus positions in 6DOF using fluoroscopic images. The accuracy of the method was evaluated under an idealized and *in vivo* test. Under idealized environment, the search space of the optimizer was constrained to a range of $\pm 5\,mm$ in translation and $\pm 5\,°$ in rotation and a range of $\pm 20\,mm$ and $\pm 20\,°$ from the ideal pose. For each range, three objective functions were tested considering humerus poses with only one rotation about one axis and humerus poses with rotations and translations about the three axes. Using idealized dual fluoroscopic images, the results showed that the minimization of the distances was the objective function which reproduced humerus poses with more accuracy and in agreement with previous studies. The minimization of the intersection areas and moments of inertia showed limited accuracy. Satisfactory results were obtained when constraining the search space to a range of $\pm 5\,mm$ and $\pm 5\,°$. However, when using a larger range as $\pm 20\,mm$ and $\pm 20\,°$, the poses were determined with a considerable error. When using single fluoroscopic images, the in-plane accuracy in determining humerus poses was satisfactory, but large out-plane errors in translation were found.

For the *in vivo* test, only a qualitative analysis of the results was performed since the actual position of the humerus is unknown. It was observed a reduced alignment between the two matching models. Following studies should take into consideration the exact magnification factor associated to the fluoroscopic images. Likely, the application of advanced image segmentation techniques for extraction of fluoroscopic contours in a future work could contribute to higher accuracies. It would be interesting to use the intensity and texture information of the acquired fluoroscopic images and the projections of the 3D bone volume during the matching process. By using all the available information on the bone, rather than its external edges alone, the accuracy of the matching method would improve, as demonstrated in [5] and [34].

This study used GA to find an optimum solution since they are more reliable in finding a global minimum than the usually used gradient-based algorithms. However, there are many operators and parameters that can be altered so that the performance of the algorithm can improve [1]. For example, an improved solution could possibly be achieved by varying the parameters of the algorithm, such as mutation probability and crossover fraction.

In conclusion, this methodology could be a useful tool for investigating the kinematics of the human body. However, more *in vivo* test should be performed to understand the limits of the applicability of the method. With further research could be readily applied to study the shoulder kinematics.

References

[1] G. C. Terry e T. M. Chopp, «Functional Anatomy of the Shoulder», *J. Athl. Train.*, vol. 35, n. 3, pp. 248–255, 2000.

[2] D. F. Massimini, J. J. P. Warner, e G. Li, «Non-invasive determination of coupled motion of the scapula and humerus—An in-vitro validation», *J. Biomech.*, vol. 44, n. 3, pp. 408–412, Fev. 2011.

[3] M. J. Bey, R. Zauel, S. K. Brock, e S. Tashman, «Validation of a New Model-Based Tracking Technique for Measuring Three-Dimensional, In Vivo Glenohumeral Joint Kinematics», *J. Biomech. Eng.*, vol. 128, n. 4, p. 604, 2006.

[4] C. Quental, J. Folgado, J. Ambrósio, e J. Monteiro, «A multibody biomechanical model of the upper limb including the shoulder girdle», *Multibody Syst. Dyn.*, vol. 28, n. 1, pp. 83–108, Ago. 2012.

[5] «Alterations in Shoulder Kinematics and Associated Muscle Activity in People With Symptoms of Shoulder Impingement», *Phys. Ther.*, Mar. 2000.

[6] L. J. Hébert, H. Moffet, B. J. McFadyen, e C. E. Dionne, «Scapular behavior in shoulder impingement syndrome», *Arch. Phys. Med. Rehabil.*, vol. 83, n. 1, pp. 60–69, Jan. 2002.

[7] J. Lin *et al.*, «Functional activity characteristics of individuals with shoulder dysfunctions», *J. Electromyogr. Kinesiol.*, vol. 15, n. 6, pp. 576–586, Dez. 2005.

[8] J.-P. Baeyens, P. Van Roy, A. De Schepper, G. Declercq, e J.-P. Clarijs, «Glenohumeral joint kinematics related to minor anterior instability of the shoulder at the end of the late preparatory phase of throwing», *Clin. Biomech.*, vol. 16, n. 9, pp. 752–757, Nov. 2001.

[9] J. Bingham e G. Li, «An Optimized Image Matching Method for Determining In-Vivo TKA Kinematics with a Dual-Orthogonal Fluoroscopic Imaging System», *J. Biomech. Eng.*, vol. 128, n. 4, p. 588, 2006.

[10] Z. Zhu e G. Li, «An automatic 2D–3D image matching method for reproducing spatial knee joint positions using single or dual fluoroscopic images», *Comput. Methods Biomech. Biomed. Engin.*, vol. 15, n. 11, pp. 1245–1256, Nov. 2012.

[11] T. Gaskill e P. J. Millett, «Snapping Scapula Syndrome: Diagnosis and Management»:, *J. Am. Acad. Orthop. Surg.*, vol. 21, n. 4, pp. 214–224, Abr. 2013.

[12] P. M. Ludewig e J. F. Reynolds, «The Association of Scapular Kinematics and Glenohumeral Joint Pathologies», *J. Orthop. Sports Phys. Ther.*, vol. 39, n. 2, pp. 90–104, Fev. 2009.

[13] M.-M. Lefèvre-Colau *et al.*, «Kinematic patterns in normal and degenerative shoulders. Part II: Review of 3-D scapular kinematic patterns in patients with shoulder pain, and clinical implications», *Ann. Phys. Rehabil. Med.*, vol. 61, n. 1, pp. 46–53, Jan. 2018.

[14] A. Tzannes, A. Paxinos, M. Callanan, e G. A. . Murrell, «An assessment of the interexaminer reliability of tests for shoulder instability», *J. Shoulder Elbow Surg.*, vol. 13, n. 1, pp. 18–23, Jan. 2004.

[15] H. Graichen *et al.*, «Magnetic Resonance Based Motion Analysis of the Shoulder During Elevation»:, *Clin. Orthop.*, vol. 370, pp. 154–163, Jan. 2000.

[16] C. W. A. Pfirrmann, M. Huser, G. Székely, J. Hodler, e C. Gerber, «Evaluation of Complex Joint Motion With Computer-Based Analysis of Fluoroscopic Sequences»:, *Invest. Radiol.*, vol. 37, n. 2, pp. 73–76, Fev. 2002.

[17] S. D. Bagg e W. J. Forrest, «A biomechanical analysis of scapular rotation during arm abduction in the scapular plane», *Am. J. Phys. Med. Rehabil.*, vol. 67, n. 6, pp. 238–245, Dez. 1988.

[18] G. R. Johnson, P. R. Stuart, e S. Mitchell, «A method for the measurement of three-dimensional scapular movement», *Clin. Biomech.*, vol. 8, n. 5, pp. 269–273, Set. 1993.

[19] P. W. McClure, L. A. Michener, B. J. Sennett, e A. R. Karduna, «Direct 3-dimensional measurement of scapular kinematics during dynamic movements in vivo», *J. Shoulder Elbow Surg.*, vol. 10, n. 3, pp. 269–277, Mai. 2001.

[20] G. Wu *et al.*, «ISB recommendation on definitions of joint coordinate systems of various joints for the reporting of human joint motion—Part II: shoulder, elbow, wrist and hand», *J. Biomech.*, vol. 38, n. 5, pp. 981–992, Mai. 2005.

[21] R. E. Debski, P. J. McMahon, W. O. Thompson, S. L.-Y. Woo, J. J. P. Warner, e F. H. Fu, «A new dynamic testing apparatus to study glenohumeral joint motion», *J. Biomech.*, vol. 28, n. 7, pp. 869–874, Jul. 1995.

[22] L. Z. Payne, X.-H. Deng, E. V. Craig, P. A. Torzilli, e R. F. Warren, «The Combined Dynamic and Static Contributions to Subacromial Impingement: A Biomechanical Analysis», *Am. J. Sports Med.*, vol. 25, n. 6, pp. 801–808, Nov. 1997.

[23] A. M. Hill, A. M. J. Bull, R. J. Dallalana, A. L. Wallace, e G. R. Johnson, «Glenohumeral motion: review of measurement techniques», *Knee Surg. Sports Traumatol. Arthrosc.*, vol. 15, n. 9, pp. 1137–1143, Ago. 2007.

[24] W. Sahara, K. Sugamoto, M. Murai, e H. Yoshikawa, «Three-dimensional clavicular and acromioclavicular rotations during arm abduction using vertically open MRI», *J. Orthop. Res.*, vol. 25, n. 9, pp. 1243–1249, Set. 2007.

[25] R. M. O. von Eisenhart-Rothe, A. Jäger, K.-H. Englmeier, T. J. Vogl, e H. Graichen, «Relevance of Arm Position and Muscle Activity on Three-Dimensional Glenohumeral Translation in Patients with Traumatic and Atraumatic Shoulder Instability <sup/>», *Am. J. Sports Med.*, vol. 30, n. 4, pp. 514–522, Jul. 2002.

[26] R. C. Rhoad *et al.*, «A new in vivo technique for three-dimensional shoulder kinematics analysis», *Skeletal Radiol.*, vol. 27, n. 2, pp. 92–97, Fev. 1998.

[27] G. A. Paletta, J. J. P. Warner, R. F. Warren, A. Deutsch, e D. W. Altchek, «Shoulder kinematics with two-plane x-ray evaluation in patients with anterior instability or rotator cuff tearing», *J. Shoulder Elbow Surg.*, vol. 6, n. 6, pp. 516–527, Nov. 1997.

[28] K. R. T. Fink e J. R. Fink, «4 - Principles of Modern Neuroimaging», em *Principles of Neurological Surgery (Fourth Edition)*, R. G. Ellenbogen, L. N. Sekhar, N. D. Kitchen, e H. B. da Silva, Eds. Philadelphia: Content Repository Only!, 2018, pp. 62-86.e2.

[29] G. Li, «Feasibility of Using Orthogonal Fluoroscopic Images to Measure In Vivo Joint Kinematics», *J. Biomech. Eng.*, vol. 126, n. 2, p. 313, Mai. 2004.

[30] G. R. Hanson, J. F. Suggs, A. A. Freiberg, S. Durbhakula, e G. Li, «Investigation of in vivo 6DOF total knee arthoplasty kinematics using a dual orthogonal fluoroscopic system», *J. Orthop. Res.*, vol. 24, n. 5, pp. 974–981, Abr. 2006.

[31] J. F. Schutte, B.-I. Koh, J. A. Reinbolt, R. T. Haftka, A. D. George, e B. J. Fregly, «Evaluation of a Particle Swarm Algorithm For Biomechanical Optimization», *J. Biomech. Eng.*, vol. 127, n. 3, p. 465, 2005.

[32] J. S. Higginson, R. R. Neptune, e F. C. Anderson, «Simulated parallel annealing within a neighborhood for optimization of biomechanical systems», *J. Biomech.*, vol. 38, n. 9, pp. 1938–1942, Set. 2005.

[33] D. Nagy, «Design optimization», *Generative Design*, 20-Mar-2017. .

[34] B.-M. You, P. Siy, W. Anderst, e S. Tashman, «In vivo measurement of 3-D skeletal kinematics from sequences of biplane radiographs: Application to knee kinematics», *IEEE Trans. Med. Imaging*, vol. 20, n. 6, pp. 514–525, Jun. 2001.

[35] Z. Zhu, D. F. Massimini, G. Wang, J. J. P. Warner, e G. Li, «The accuracy and repeatability of an automatic 2D–3D fluoroscopic image-model registration technique for determining shoulder joint kinematics», *Med. Eng. Phys.*, vol. 34, n. 9, pp. 1303–1309, Nov. 2012.

[36] S. Widnall, «3D Rigid Body Dynamics: The Inertia Tensor», p. 13.

[37] C. C. Pagano, M. T. Turvey, e J. Gibson, «The Inertia Tensor as a Basis for the Perception of Limb Orientation», p. 18.

[38] R. R. Carlton e A. M. Adler, *Principles of Radiographic Imaging: An Art and A Science*. Cengage Learning, 2012.

[39] H. Gray, Gray's Anatomy 20th Edition, 1918.

[40] T. Hendrickson. "Chapter 6: The Shoulder - Anatomy, Function, and Dysfunction of the Shoulder Complex." p. 239–91 in Massage and Manual Therapy for Orthopedic Conditions, 2009.

[41] Kimberly A. Szucs, M.S., OTR/L, ''Capturing Three-Dimensional Clavicle Kinematics During Arm Elevation: Describing the Contribution of Clavicle Motion and Associated Scapulothoracic Muscle Activation to Total Shoulder Complex Motion'', *The Ohio State University*, 2010

[42] S. Gutiérrez, I.P. Pappou, J.Aira, P. Simon, M.A. Frankle (2018). "Chapter 2: Biomechanics of the Clavicle". p.19-32 in Clavicle Injuries.

[43] J. S Arora. Introduction to Optimum design, 2011.

[44] K. M. Dyce, W. O. Sack, e C. J. G. Wensing, BOPOD - Textbook of Veterinary Anatomy. Elsevier Health Sciences, 2009.

Appendix

A. Range of $\pm$ 5 mm in translation and $\pm$ 5 ° in rotation

A.1. Minimization of the intersection areas

Table A.1.1 –20 optimizations and respective final value of the objective function *Fval* for the five poses when using idealized dual fluoroscopic images for minimization of the intersection areas under the range of [$\pm 5\ mm;\ \pm 5\ °$] .

	α (°)	β (°)	γ (°)	x (mm)	y (mm)	z (mm)	*Fval*
SP1	0,006	0,012	0,031	-0,001	0,002	0,000	6,29E-01
	0,013	0,017	0,052	-0,004	0,003	0,000	1,89E+00
	0,000	0,145	0,535	-0,032	-0,013	0,001	1,70E+02
	0,018	0,234	0,759	-0,055	-0,007	-0,010	3,11E+02
	0,009	0,009	0,041	-0,002	0,003	0,000	8,85E-01
	0,001	0,003	0,010	-0,001	0,000	0,000	1,13E-02
	0,007	0,008	0,033	-0,001	0,002	0,000	5,42E-01
	0,026	-0,264	2,405	-0,441	-0,039	0,085	3,81E+02
	0,006	0,006	0,028	-0,001	0,002	0,000	3,60E-01
	0,017	-0,338	1,595	-0,200	-0,042	-0,084	2,22E+02
	0,018	-0,373	1,610	-0,172	-0,043	-0,088	2,27E+02
	0,004	0,009	0,024	-0,002	0,001	-0,001	2,94E-01
	-0,020	0,015	0,063	-0,003	-0,005	0,002	9,47E+00
	0,027	0,547	1,975	-0,128	-0,025	-0,022	7,82E+02
	0,008	0,141	0,724	-0,058	-0,016	0,004	2,24E+02
	0,010	0,010	0,044	-0,002	0,003	0,000	1,01E+00
	0,023	-0,321	1,652	0,060	-0,026	0,046	1,97E+02
	0,083	0,938	4,365	-0,159	-0,021	-0,056	1,92E+03
	0,009	0,351	1,428	-0,072	-0,026	-0,007	4,80E+02
	0,012	0,009	0,046	-0,001	0,003	0,000	1,41E+00
SP2	59,612	0,219	1,385	0,005	0,006	0,006	3,06E+01
	59,578	0,384	2,414	0,008	0,005	0,028	7,22E+01
	59,568	0,353	2,209	0,011	0,009	0,021	6,48E+01
	59,551	0,495	2,646	-0,034	0,008	0,034	1,06E+02
	59,605	0,385	2,112	-0,021	0,005	0,007	8,05E+01
	59,559	0,371	2,391	0,016	0,008	0,030	7,07E+01
	59,683	0,008	0,073	-0,002	0,001	0,002	1,66E-01
	59,654	0,139	0,847	0,001	0,002	-0,002	2,41E+01
	59,625	0,247	1,389	-0,008	0,004	0,005	3,26E+01
	59,603	0,221	1,372	-0,001	0,007	0,010	3,05E+01
	59,685	0,016	0,081	-0,001	0,000	0,001	1,16E-01
	59,614	0,222	1,386	0,002	0,005	0,006	3,07E+01
	59,643	0,171	1,042	-0,001	0,004	0,006	2,86E+01
	59,612	0,225	1,381	0,001	0,005	0,007	3,06E+01
	59,570	0,352	2,215	0,012	0,009	0,021	6,50E+01
	59,613	0,225	1,383	0,000	0,005	0,006	3,06E+01
	59,610	0,222	1,380	0,002	0,006	0,007	3,05E+01
	59,691	0,121	0,346	-0,011	-0,002	-0,014	1,33E+01
	59,679	0,052	0,246	-0,008	0,001	0,000	1,32E+00
	59,592	0,369	2,242	0,002	0,006	0,020	6,69E+01
SP3	29,770	0,121	0,621	-0,010	-0,019	-0,023	7,82E+00
	30,105	0,714	3,870	-0,030	0,266	-0,185	1,01E+02
	30,078	0,708	3,607	-0,077	0,262	-0,156	9,22E+01
	29,865	0,699	3,163	-0,113	-0,031	0,017	5,96E+01
	29,767	0,071	0,342	-0,006	-0,029	0,000	2,67E+00
	30,197	0,360	1,969	-0,018	0,330	-0,186	1,27E+02
	30,334	0,795	3,977	-0,058	0,624	-0,086	2,26E+02
	30,049	0,654	3,386	-0,051	0,252	-0,136	7,22E+01
	30,046	0,424	2,291	-0,034	0,243	-0,113	9,63E+01
	29,954	0,610	3,066	-0,041	0,071	-0,082	3,53E+01
	29,678	0,605	3,034	0,004	-0,178	0,244	4,79E+01
	29,743	0,236	1,300	-0,002	0,002	0,014	2,04E+01
	30,078	0,601	3,390	0,019	0,253	-0,166	7,78E+01
	29,844	0,636	3,413	-0,034	-0,050	-0,057	4,79E+01
	29,883	0,704	3,874	-0,028	-0,035	0,015	6,86E+01
	29,764	0,248	1,343	-0,012	0,017	-0,003	2,13E+01
	29,899	0,715	3,882	-0,038	-0,018	0,001	7,05E+01
	29,712	0,133	2,595	-0,356	-0,653	2,041	4,94E-06
	29,712	0,737	3,523	-0,095	-0,193	0,200	6,03E+01
	29,864	0,654	3,398	-0,054	-0,046	0,034	5,13E+01
RGP1	102,475	-37,441	-111,582	8,313	-11,257	12,998	1,57E+01
	100,156	-39,194	-110,472	8,231	-11,523	12,886	1,41E+01
	103,256	-35,241	-111,825	8,002	-9,255	12,533	2,52E+01
	103,852	-36,345	-112,253	8,355	-11,105	13,055	2,33E+01
	103,443	-37,627	-112,196	8,590	-12,319	13,429	2,69E+01
	102,413	-36,874	-111,512	8,243	-11,588	12,993	1,65E+01
	102,924	-35,515	-111,661	7,992	-9,312	12,540	2,04E+01
	102,662	-36,686	-111,623	8,278	-11,588	13,033	2,34E+01
	104,445	-36,493	-112,647	8,484	-12,508	13,228	2,94E+01
	101,637	-36,520	-110,992	7,960	-9,584	12,504	1,28E+01
	103,905	-36,239	-112,208	8,220	-11,168	12,745	2,33E+01
	104,203	-37,241	-112,578	8,637	-12,669	13,455	3,02E+01
	100,097	-37,847	-110,253	7,912	-11,595	12,439	8,22E+00
	102,747	-35,386	-111,578	8,000	-9,766	12,607	3,23E+01
	101,737	-37,272	-111,100	8,070	-10,133	12,605	7,09E+00
	101,712	-36,415	-110,973	7,959	-11,543	12,466	8,73E+01
	101,276	-37,234	-110,878	8,031	-11,444	12,630	5,35E+00
	103,915	-36,305	-112,291	8,300	-10,560	12,961	2,20E+01
	99,257	-39,422	-110,117	8,013	-12,048	12,606	9,94E+01
	103,958	-36,957	-112,301	8,425	-12,776	13,063	2,74E+01
RGP2	-93,073	53,883	-97,989	14,734	8,698	17,319	6,47E-03
	-93,223	53,731	-98,003	14,733	8,698	17,320	8,83E-02
	-94,961	51,950	-98,191	14,730	8,697	17,325	1,49E+01
	-93,353	53,598	-98,019	14,734	8,699	17,320	2,27E-01
	-93,587	53,356	-98,045	14,734	8,697	17,322	1,03E+00
	-96,007	50,887	-98,313	14,728	8,695	17,326	2,84E+01
	-93,511	53,436	-98,033	14,733	8,698	17,320	5,72E-01
	-93,551	53,400	-98,025	14,732	8,698	17,321	1,75E+00
	-94,760	52,159	-98,163	14,731	8,697	17,324	1,36E+01
	-91,451	55,550	-97,828	14,737	8,703	17,323	1,45E+02
	-93,982	52,953	-98,083	14,732	8,697	17,323	2,27E+00
	-93,399	53,549	-98,024	14,734	8,697	17,321	2,87E-01
	-93,153	53,803	-97,999	14,735	8,698	17,321	8,13E-02
	-95,392	51,509	-98,252	14,729	8,696	17,328	2,08E+01
	-93,292	53,659	-98,012	14,734	8,698	17,320	1,37E-01
	-92,579	54,390	-97,940	14,736	8,699	17,319	7,81E+00
	-93,267	53,685	-98,009	14,734	8,698	17,319	1,14E-01
	-91,947	55,045	-97,875	14,736	8,704	17,316	6,52E+01
	-93,462	53,486	-98,029	14,734	8,698	17,320	4,80E-01
	-92,179	54,803	-97,901	14,737	8,701	17,318	3,81E+01

A.2. Minimization of the moments of inertia

Table A.2.1. –20 optimizations and respective final value of the objective function *Fval* for the five poses when using idealized dual fluoroscopic images for minimization of the moments of inertia under the range of $[\pm 5\ mm;\ \pm 5\ °]$.

	α (°)	β (°)	γ (°)	*Fval*
SP1	-0,185	-0,203	-0,309	4,42E-05
	-0,037	0,117	-0,023	2,05E-05
	1,069	-0,918	0,688	3,87E-04
	0,063	-0,615	-0,655	4,48E-05
	0,428	-0,156	0,869	9,52E-05
	-0,244	0,823	-0,349	1,13E-04
	0,093	0,575	-0,234	1,82E-04
	0,453	-0,052	0,710	2,64E-05
	-0,201	0,044	-0,327	7,37E-05
	0,821	-0,338	0,454	2,12E-04
	1,514	0,398	4,953	2,57E-04
	0,428	0,139	0,746	1,94E-05
	0,294	-0,091	-0,332	6,98E-05
	0,061	-0,092	-0,132	5,45E-05
	0,474	0,540	0,656	3,32E-05
	0,537	-0,354	0,762	7,53E-05
	0,814	-0,153	0,458	2,58E-04
	-0,035	-0,110	-0,386	3,38E-05
	0,289	-0,161	1,097	7,62E-04
	0,608	0,382	0,483	9,91E-05
SP2	59,668	-0,304	-0,222	2,74E-05
	59,124	-0,185	0,032	3,96E-04
	59,614	-0,167	-0,247	1,61E-04
	59,405	-0,613	-0,599	7,24E-05
	59,980	-0,652	-1,476	7,48E-04
	59,597	0,052	0,145	1,87E-05
	59,668	-0,636	-1,948	5,81E-04
	59,706	0,219	0,384	4,23E-05
	59,660	0,038	0,058	2,45E-05
	59,612	-0,445	-0,386	1,66E-06
	59,955	-0,456	-0,339	3,33E-04
	59,954	-0,766	-0,976	4,61E-04
	59,838	-0,451	-1,883	6,07E-05
	59,739	-0,528	-2,102	1,71E-04
	59,442	-0,480	-0,316	2,43E-05
	59,580	-0,353	-0,343	3,80E-05
	59,732	0,017	-0,047	8,85E-05
	59,625	-0,053	0,154	4,77E-05
	59,595	-0,147	0,053	7,09E-05
	60,299	-1,064	-1,358	1,60E-03
SP3	30,183	-0,254	-0,011	1,20E-05
	29,932	-0,144	-0,569	4,82E-05
	30,024	0,103	-0,215	1,56E-05
	29,824	0,012	0,000	2,56E-05
	29,919	0,441	-0,068	1,74E-05
	29,642	0,280	-0,121	3,48E-05
	30,031	0,099	-0,382	3,70E-05
	30,112	0,259	0,328	4,27E-05
	29,739	-0,596	1,324	1,32E-05
	30,037	-0,331	-0,265	6,92E-05
	29,910	0,322	0,201	2,41E-05
	29,385	0,204	1,498	4,55E-06
	30,019	0,411	1,592	5,57E-05
	29,762	0,037	0,094	7,64E-06
	29,913	0,203	0,013	1,41E-05
	29,851	-0,098	-0,090	3,77E-06
	30,005	-0,158	-0,433	1,12E-05
	28,882	-0,910	1,182	1,21E-04
	29,844	0,344	0,030	2,57E-05
	30,194	-0,554	-0,013	2,87E-05
RGP1	99,431	-38,129	-109,936	5,13E-05
	99,647	-37,483	-110,790	2,99E-04
	99,236	-39,411	-109,507	8,73E-05
	98,268	-37,763	-110,725	2,07E-04
	99,215	-38,208	-109,861	3,99E-05
	98,867	-39,438	-109,437	6,61E-05
	98,552	-40,062	-109,237	1,22E-04
	98,574	-39,132	-108,487	5,60E-05
	99,145	-39,170	-109,559	3,59E-05
	98,670	-38,831	-108,916	1,06E-04
	99,647	-39,068	-109,669	3,18E-05
	98,662	-38,504	-108,825	1,30E-06
	99,893	-37,072	-110,670	3,19E-04
	98,868	-40,165	-112,177	1,52E-04
	98,200	-37,582	-110,777	2,37E-04
	97,101	-39,195	-108,578	2,17E-04
	99,944	-37,363	-111,074	2,54E-04
	99,236	-39,076	-109,602	2,31E-05
	99,369	-40,115	-112,531	3,03E-04
	98,874	-39,197	-109,418	1,03E-04
RGP2	-91,237	58,600	-97,081	6,70E-04
	-93,565	53,146	-98,410	2,46E-05
	-92,769	53,225	-97,504	1,80E-04
	-90,802	55,063	-98,495	2,18E-04
	-92,673	53,476	-98,056	6,69E-05
	-95,514	54,661	-98,442	3,41E-04
	-94,025	52,707	-97,320	1,19E-04
	-88,214	57,200	-98,089	1,10E-04
	-89,175	57,523	-97,434	1,43E-04
	-88,464	57,053	-97,932	1,92E-05
	-96,970	50,477	-98,383	2,10E-04
	-94,190	52,960	-98,440	1,44E-04
	-90,585	55,876	-97,857	1,28E-04
	-92,365	55,178	-97,636	1,75E-05
	-95,232	51,506	-98,520	1,26E-04
	-89,206	56,399	-98,344	1,06E-04
	-93,932	52,523	-98,554	3,38E-04
	-94,624	54,607	-98,047	4,19E-04
	-94,580	54,499	-97,612	3,14E-04
	-93,321	52,842	-97,194	2,29E-04

A.3. Minimization of the distances

Table A.3.1. –20 optimizations and respective final value of the objective function *Fval* for the five poses when using idealized dual fluoroscopic images for minimization of the distances under the range of $[\pm 5\ mm;\ \pm 5\ ^{\circ}]$.

	α (°)	β (°)	γ (°)	x (mm)	y (mm)	z (mm)	*Fval*
SP1	0,000	0,009	0,028	0,000	0,001	0,000	3,02E-04
	0,002	-0,001	-0,005	0,001	0,000	0,000	4,41E-06
	-0,014	0,075	0,130	-0,005	0,001	0,002	3,59E-05
	0,060	0,028	0,011	-0,003	0,008	-0,002	1,50E-06
	0,003	-0,001	-0,003	0,001	0,000	0,000	5,36E-05
	0,009	0,038	0,093	-0,002	0,003	0,000	1,15E-03
	-0,010	0,007	0,038	0,001	0,003	0,000	2,80E-04
	0,005	0,000	0,007	0,001	0,001	0,000	2,59E-05
	0,025	0,015	0,039	-0,001	0,004	0,002	4,02E-05
	0,011	0,007	0,034	0,000	0,002	0,000	3,04E-05
	-0,007	0,117	0,109	-0,014	0,002	-0,001	1,87E-06
	-0,001	0,009	0,011	0,003	0,002	0,000	3,52E-05
	0,003	0,001	0,008	0,000	0,001	0,000	1,20E-06
	0,022	0,006	0,039	0,000	0,004	-0,001	1,79E-04
	0,002	0,007	0,035	0,000	0,001	0,000	1,50E-05
	0,003	0,038	0,049	-0,002	0,002	0,001	1,01E-03
	0,010	0,010	0,038	-0,001	0,003	0,000	4,02E-05
	-0,001	0,003	0,018	0,000	0,001	0,000	9,67E-05
	0,000	0,005	0,039	0,001	0,002	0,000	2,71E-05
	0,005	0,012	0,045	-0,002	0,003	0,000	2,47E-03
SP2	59,689	0,002	0,002	0,000	0,000	0,000	3,34E-04
	59,689	0,016	0,015	-0,001	0,001	0,000	1,61E-05
	59,692	0,007	0,013	0,000	0,000	0,000	3,10E-05
	59,694	0,011	0,011	-0,001	0,000	0,000	3,21E-06
	59,690	0,046	0,053	-0,001	-0,001	-0,001	1,20E-06
	59,698	0,010	-0,003	-0,001	0,001	0,000	3,05E-03
	59,695	0,002	0,044	0,000	0,001	0,000	2,64E-05
	59,696	-0,004	0,005	0,001	0,000	-0,001	1,14E-03
	59,697	0,000	0,001	-0,001	0,000	0,000	9,96E-05
	59,693	-0,011	0,039	0,002	-0,002	0,000	2,83E-03
	59,709	0,002	0,018	0,001	0,001	-0,002	3,71E-05
	59,692	0,002	-0,001	0,000	0,000	0,000	2,99E-05
	59,691	0,000	0,004	0,000	0,000	-0,001	1,33E-03
	59,692	0,006	0,010	0,000	0,000	-0,001	3,77E-04
	59,694	-0,006	0,008	0,000	0,000	0,000	2,92E-04
	59,701	0,012	0,047	0,002	0,001	-0,001	1,21E-04
	59,691	0,001	0,002	0,000	0,000	0,000	6,49E-05
	59,725	0,006	0,017	0,000	0,001	-0,003	1,00E-05
	59,691	-0,002	-0,010	0,000	0,000	0,000	1,88E-05
	59,690	0,003	0,004	0,000	-0,001	0,000	1,70E-04
SP3	29,846	-0,001	-0,002	0,000	0,000	0,000	9,80E-06
	29,844	-0,004	-0,007	0,000	0,000	0,000	5,61E-04
	29,836	0,005	-0,005	-0,002	-0,001	0,000	8,67E-04
	29,844	0,010	0,004	-0,002	0,002	0,000	3,08E-05
	29,847	-0,007	-0,006	0,001	0,000	0,001	6,33E-03
	29,847	-0,002	-0,010	-0,001	0,000	0,000	3,42E-04
	29,845	-0,001	-0,005	0,000	0,001	0,001	8,26E-04
	29,851	-0,001	-0,016	-0,002	0,002	0,000	6,54E-05
	29,833	-0,002	-0,002	0,000	0,002	0,001	5,65E-04
	29,851	0,004	0,002	0,000	0,001	0,000	4,63E-02
	29,843	0,168	0,138	-0,027	0,002	0,000	1,38E-03
	29,851	0,087	0,023	-0,015	0,001	-0,001	8,43E-02
	29,852	0,022	0,006	-0,004	0,001	0,000	1,89E-03
	29,844	0,155	0,119	-0,024	0,002	0,000	7,63E-05
	29,848	0,010	-0,006	-0,001	0,000	0,000	2,13E-02
	29,846	0,022	0,008	-0,003	0,000	0,000	3,31E-04
	29,847	0,002	-0,007	-0,001	0,001	0,000	6,00E-04
	29,846	0,006	0,003	-0,001	0,000	0,000	4,37E-03
	29,844	0,005	-0,002	-0,001	0,000	0,000	1,36E-03
	29,848	0,004	0,002	-0,001	0,000	0,000	4,48E-02
RGP1	99,635	-38,247	-110,016	7,898	-11,611	12,413	7,92E-05
	99,549	-38,329	-110,010	7,897	-11,612	12,411	5,90E-03
	99,602	-38,280	-110,032	7,897	-11,611	12,413	6,55E-04
	99,553	-38,322	-110,002	7,896	-11,612	12,412	1,15E-01
	99,699	-38,160	-109,979	7,900	-11,604	12,418	2,96E-03
	99,614	-38,245	-110,017	7,898	-11,606	12,413	1,30E-02
	99,884	-38,039	-110,115	7,904	-11,613	12,421	1,24E-02
	99,714	-38,223	-110,024	7,899	-11,620	12,408	1,86E-03
	99,891	-38,081	-110,178	7,902	-11,617	12,421	7,08E-06
	99,546	-38,329	-109,999	7,896	-11,611	12,411	6,22E-04
	99,573	-38,303	-110,012	7,896	-11,611	12,413	1,36E-02
	99,819	-38,079	-110,091	7,902	-11,610	12,421	5,47E-03
	99,740	-38,186	-110,100	7,903	-11,615	12,423	8,91E-04
	99,881	-38,036	-110,126	7,903	-11,612	12,420	1,51E-03
	99,525	-38,355	-110,013	7,898	-11,610	12,413	6,91E-05
	99,869	-38,065	-110,132	7,903	-11,613	12,421	2,73E-04
	99,542	-38,333	-110,002	7,895	-11,612	12,412	3,95E-04
	99,689	-38,204	-110,012	7,900	-11,611	12,419	3,04E-03
	99,540	-38,330	-109,977	7,896	-11,611	12,411	1,41E-02
	99,539	-38,333	-110,001	7,895	-11,611	12,412	2,21E-03
RGP2	-91,366	55,614	-97,800	14,739	8,697	17,319	2,74E-04
	-91,655	55,322	-97,846	14,739	8,698	17,321	1,19E-04
	-92,663	54,294	-97,940	14,735	8,697	17,319	1,17E-03
	-91,876	55,096	-97,853	14,737	8,696	17,320	2,84E-03
	-92,843	54,118	-97,962	14,734	8,698	17,319	7,75E-02
	-93,188	53,759	-97,992	14,735	8,701	17,319	6,71E-03
	-93,094	53,860	-97,986	14,734	8,697	17,319	2,85E-04
	-92,691	54,269	-97,944	14,735	8,697	17,319	4,86E-02
	-93,560	53,381	-98,026	14,736	8,699	17,319	5,68E-04
	-92,879	54,079	-97,962	14,734	8,696	17,319	1,13E-01
	-92,208	54,762	-97,899	14,738	8,698	17,320	7,59E-04
	-92,946	54,014	-97,977	14,735	8,698	17,319	1,69E-05
	-91,856	55,120	-97,856	14,738	8,698	17,320	2,64E-02
	-92,407	54,564	-97,907	14,736	8,699	17,320	5,61E-04
	-93,584	53,363	-98,034	14,733	8,698	17,319	8,33E-03
	-92,477	54,460	-97,927	14,735	8,692	17,322	8,77E-03
	-92,085	54,886	-97,842	14,734	8,696	17,319	1,03E-03
	-91,618	55,359	-97,840	14,739	8,698	17,321	1,73E-02
	-92,868	54,096	-97,970	14,735	8,699	17,318	1,92E-02
	-93,538	53,412	-98,020	14,733	8,699	17,318	1,55E-02

B. Range of $\pm$ 20 mm in translation and $\pm 20°$ in rotation

B.1. Minimization of the areas

Table B.1.1 –20 optimizations and respective final value of the objective function *Fval* for the five poses when using idealized dual fluoroscopic images for minimization of the areas under the range of [$\pm 20\ mm;\ \pm 20\ °$] .

	α (°)	β (°)	γ (°)	x (mm)	y (mm)	z (mm)	*Fval*
SP1	0,049	1,076	4,325	-0,228	-0,033	-0,036	1,91E+03
	0,005	0,294	1,166	-0,061	-0,023	-0,004	3,90E+02
	0,007	1,544	1,447	-0,372	-0,140	-0,098	1,33E+04
	0,046	0,999	4,322	-0,208	-0,037	-0,041	1,80E+03
	0,038	0,426	1,691	-0,089	-0,015	-0,013	5,87E+02
	0,012	0,928	4,277	-0,170	-0,055	-0,037	1,59E+03
	0,008	0,009	0,024	-0,001	0,001	0,000	8,71E-01
	0,010	0,011	0,046	-0,002	0,003	0,000	1,13E+00
	0,125	1,013	4,430	-0,190	-0,002	-0,057	2,26E+03
	0,006	0,006	0,018	-0,002	0,002	0,000	4,05E-01
	0,003	0,365	1,434	-0,078	-0,031	-0,006	4,94E+02
	0,079	0,228	0,742	-0,044	0,017	-0,002	3,78E+02
	0,047	0,935	4,319	-0,174	-0,036	-0,047	1,78E+03
	0,007	0,211	0,965	-0,052	-0,018	-0,003	3,38E+02
	0,050	1,042	4,330	-0,220	-0,033	-0,034	1,84E+03
	0,006	0,267	0,936	-0,060	-0,017	-0,005	3,60E+02
	0,045	1,010	4,328	-0,205	-0,032	-0,038	1,89E+03
	0,005	0,929	4,271	-0,171	-0,058	-0,033	1,56E+03
	0,006	0,138	0,551	-0,030	-0,014	-0,005	1,63E+02
	0,015	0,013	0,052	-0,003	0,003	0,001	2,22E+00
SP2	59,093	1,761	10,022	-0,044	0,076	0,073	6,23E+02
	58,913	2,502	13,158	-0,155	0,090	0,094	1,03E+03
	59,134	1,622	9,543	-0,003	0,066	0,074	5,86E+02
	59,158	1,771	10,039	-0,060	0,065	0,078	6,29E+02
	59,013	1,999	10,956	-0,095	0,076	0,080	7,27E+02
	59,107	1,729	9,891	-0,035	0,068	0,087	6,16E+02
	58,999	1,979	10,599	-0,140	0,092	0,070	7,06E+02
	59,109	1,759	10,209	-0,012	0,070	0,081	6,28E+02
	59,128	1,680	9,693	-0,035	0,064	0,096	6,02E+02
	59,071	1,841	10,096	-0,107	0,083	0,078	6,43E+02
	59,060	2,056	11,735	-0,027	0,077	0,077	7,99E+02
	59,057	1,503	9,289	0,080	0,062	0,099	5,55E+02
	59,095	1,790	10,080	-0,074	0,084	0,097	6,32E+02
	59,075	1,813	10,008	-0,091	0,078	0,074	6,32E+02
	59,166	1,579	9,495	0,031	0,058	0,076	5,74E+02
	59,149	1,399	9,132	0,162	0,063	0,091	5,48E+02
	59,081	1,769	10,071	-0,041	0,078	0,073	6,28E+02
	59,204	1,565	9,518	0,061	0,055	0,069	5,78E+02
	59,148	1,395	9,124	0,154	0,067	0,092	5,47E+02
	59,074	1,831	10,077	-0,103	0,078	0,080	6,40E+02
SP3	30,112	1,627	8,437	-0,139	0,257	-0,097	7,49E+02
	29,779	-0,128	2,933	-0,129	-0,771	2,242	1,20E-06
	29,799	2,660	13,871	-0,304	-0,531	0,570	1,56E+03
	28,588	3,447	15,820	-0,494	-0,279	0,113	2,82E+03
	29,996	0,718	3,989	-0,020	0,091	-0,090	8,81E+01
	28,863	3,151	15,740	-0,323	-0,063	-0,119	2,42E+03
	28,231	4,045	18,710	-0,502	0,682	0,329	3,70E+03
	30,255	4,413	19,797	-0,580	-0,232	-0,053	4,36E+03
	29,699	2,889	13,994	-0,458	-0,549	0,566	1,52E+03
	30,075	0,957	4,918	-0,088	0,262	-0,159	3,13E+02
	30,326	0,583	3,244	-0,051	0,448	-0,067	3,37E+02
	30,101	1,656	8,438	-0,163	0,289	-0,064	7,58E+02
	29,874	0,617	3,368	-0,028	-0,015	-0,085	5,00E+01
	29,046	4,483	19,262	-0,720	0,111	0,725	3,67E+03
	30,223	1,414	7,447	-0,110	0,352	-0,219	6,94E+02
	29,553	2,353	13,464	-0,070	0,001	0,077	2,06E+03
	29,849	1,644	8,442	-0,161	-0,009	0,058	6,38E+02
	29,011	4,426	19,348	-0,746	-2,127	1,247	3,15E+03
	30,524	1,188	6,514	-0,057	0,628	-0,343	7,38E+02
	30,140	3,568	15,726	-0,560	0,108	0,067	3,47E+03
RGP1	104,944	-35,516	-112,884	8,396	-10,866	13,131	3,39E+01
	109,581	-32,901	-115,866	8,904	-12,347	13,986	2,24E+02
	112,469	-32,257	-117,755	9,706	-10,045	15,133	6,70E+02
	112,073	-27,384	-117,895	8,325	-11,348	12,872	1,77E+03
	108,718	-33,672	-115,210	8,768	-12,455	13,701	1,20E+02
	106,309	-34,477	-113,637	8,329	-10,501	13,006	4,91E+01
	110,665	-30,934	-116,668	8,604	-10,746	13,505	2,17E+02
	110,987	-28,419	-116,947	8,302	-11,371	12,881	1,52E+03
	111,398	-30,803	-116,986	8,440	-11,629	13,083	2,50E+02
	105,811	-34,676	-112,842	8,351	-10,350	12,814	1,64E+02
	104,270	-35,875	-112,364	8,159	-11,266	12,622	2,71E+01
	112,106	-27,346	-117,888	8,332	-11,347	12,849	1,80E+03
	109,945	-32,114	-116,024	8,504	-12,320	13,301	1,73E+02
	111,798	-27,607	-117,647	8,294	-11,352	12,827	1,69E+03
	105,237	-36,986	-112,789	8,799	-9,933	13,599	1,23E+02
	112,438	-31,738	-117,395	8,516	-10,336	13,025	5,38E+02
	112,243	-31,786	-117,374	7,605	-9,113	11,648	2,25E+03
	104,993	-33,415	-112,623	8,059	-11,352	12,519	5,59E+02
	107,340	-33,363	-113,947	8,070	-11,305	12,391	5,93E+02
	112,752	-26,935	-118,528	8,310	-11,319	12,875	2,01E+03
RGP2	-91,532	55,487	-97,733	14,716	8,712	17,319	**2,76E+02**
	-91,980	55,010	-97,881	14,739	8,703	17,318	6,01E+01
	-93,059	53,897	-97,987	14,734	8,698	17,319	7,66E-03
	-88,997	58,102	-97,607	14,743	8,711	17,345	1,53E+03
	-93,226	53,728	-98,003	14,733	8,698	17,319	1,02E-01
	-94,967	51,945	-98,189	14,729	8,695	17,324	1,49E+01
	-93,410	53,541	-98,016	14,730	8,698	17,321	5,79E-01
	-92,528	54,443	-97,934	14,735	8,700	17,319	9,90E+00
	-94,350	52,573	-98,141	14,735	8,695	17,328	6,36E+00
	-95,409	51,484	-98,259	14,736	8,687	17,332	2,25E+01
	-94,132	52,804	-98,098	14,731	8,698	17,322	2,92E+00
	-92,888	54,075	-97,947	14,729	8,699	17,318	4,37E+00
	-92,873	54,088	-97,969	14,735	8,699	17,319	7,39E-01
	-94,087	52,847	-98,097	14,732	8,698	17,322	2,75E+00
	-94,183	52,768	-98,087	14,729	8,707	17,333	6,64E+00
	-93,124	53,830	-97,994	14,734	8,698	17,319	2,69E-02
	-91,423	55,587	-97,826	14,739	8,707	17,319	1,52E+02
	-92,393	54,582	-97,921	14,736	8,700	17,319	1,72E+01
	-93,980	52,954	-98,079	14,731	8,698	17,323	2,39E+00
	-90,876	56,162	-97,712	14,735	8,715	17,315	3,91E+02

B.2. Minimization of the moments of inertia

Table B.2.1. –20 optimizations and respective final value of the objective function *Fval* for the five poses when using idealized dual fluoroscopic images for minimization of the moments of inertia under the range of $[\pm 20\ mm;\ \pm 20\ ^\circ]$.

	α (°)	β (°)	γ (°)	*Fval*
SP1	-2,914	-1,082	4,301	3,92E-03
	-2,432	-0,697	-0,506	7,28E-05
	-0,025	0,681	-0,430	1,26E-04
	-1,833	1,865	4,144	4,38E-04
	-2,704	-1,804	-1,145	2,75E-04
	2,594	-0,312	2,552	2,79E-04
	-0,822	1,176	-0,299	2,39E-04
	1,679	-3,604	-5,283	1,99E-04
	-1,708	3,600	4,168	2,20E-03
	1,991	-1,004	0,662	5,48E-04
	1,384	1,704	3,933	3,65E-04
	1,948	1,472	3,789	9,78E-05
	0,073	0,138	-0,619	3,64E-05
	0,748	2,037	19,774	6,57E-05
	1,261	1,665	4,040	5,08E-04
	-0,121	1,507	0,247	1,13E-03
	1,771	-3,519	-6,095	2,34E-05
	-0,894	1,539	2,809	1,85E-05
	0,173	0,240	-0,176	2,01E-04
	-1,465	3,682	19,645	1,14E-03
SP2	59,273	0,468	-6,441	3,13E-03
	61,423	-0,374	-1,490	3,56E-04
	58,725	-2,247	-10,824	7,40E-05
	57,497	1,610	12,264	4,49E-03
	60,120	-3,119	-6,050	2,00E-03
	59,957	0,407	0,536	6,19E-04
	57,618	-2,069	-11,082	2,91E-03
	62,650	-2,020	-2,913	1,97E-03
	58,471	-0,688	-9,891	1,80E-03
	57,065	-0,955	-4,768	3,55E-03
	57,757	-1,062	-9,555	1,86E-03
	60,917	0,914	12,965	1,12E-03
	59,301	0,238	11,787	2,25E-03
	62,578	-1,466	-10,855	2,05E-03
	59,750	-2,910	-12,173	2,05E-03
	62,807	-0,357	-0,292	6,50E-04
	61,425	0,074	0,729	2,54E-03
	60,253	0,990	1,133	5,76E-04
	60,214	-0,387	-9,946	8,12E-05
	59,248	-0,844	-0,743	1,08E-04
SP3	28,301	2,402	2,529	2,50E-03
	29,786	0,763	5,010	9,28E-05
	29,598	-0,358	1,763	2,83E-04
	30,075	-0,837	-0,422	1,44E-04
	30,915	0,267	-1,010	2,21E-04
	30,311	0,951	-0,177	2,61E-04
	30,997	0,985	-0,504	1,40E-04
	30,536	-0,705	0,039	2,87E-04
	30,224	0,926	5,162	1,43E-04
	29,013	0,505	1,031	1,26E-03
	31,027	0,901	-0,600	1,37E-04
	28,423	-0,593	3,277	9,00E-04
	31,602	0,747	-0,731	6,61E-04
	29,770	-0,282	-0,506	1,22E-04
	29,703	-0,392	0,590	4,06E-05
	29,476	-0,619	0,779	2,37E-04
	31,120	0,704	-0,874	2,60E-04
	31,240	1,490	0,362	1,76E-03
	30,108	-0,257	-0,011	9,08E-05
	29,731	0,074	-0,099	5,58E-05
RGP1	100,974	-37,311	-111,438	1,15E-03
	106,827	-22,393	-106,248	4,39E-03
	94,394	-39,765	-110,309	5,17E-04
	96,425	-37,819	-110,477	8,63E-04
	96,544	-36,412	-110,918	2,19E-03
	102,015	-35,518	-110,593	2,91E-03
	96,532	-39,615	-111,258	2,27E-04
	98,728	-39,772	-107,850	2,54E-04
	93,402	-39,722	-109,829	5,84E-04
	96,643	-37,573	-110,497	8,26E-04
	81,953	-42,466	-93,658	9,13E-04
	99,880	-39,178	-109,792	1,07E-04
	98,946	-40,283	-112,451	2,32E-04
	104,767	-26,946	-113,348	6,11E-03
	96,888	-42,616	-107,016	6,83E-04
	100,979	-25,690	-100,256	4,98E-03
	105,993	-21,220	-105,621	1,02E-02
	102,328	-31,260	-111,549	4,70E-03
	95,446	-42,938	-106,472	2,52E-03
	84,580	-43,048	-108,872	2,24E-03
RGP2	-82,884	62,338	-99,300	1,53E-04
	-86,345	58,764	-95,463	3,66E-03
	-80,383	64,540	-97,666	4,81E-04
	-74,708	69,597	-102,871	5,10E-03
	-84,780	65,659	-95,493	4,57E-04
	-87,657	56,396	-98,574	2,96E-03
	-96,456	47,912	-97,972	5,15E-04
	-96,094	50,225	-98,317	7,49E-05
	-84,297	65,995	-95,172	4,99E-04
	-102,861	46,090	-97,494	5,26E-04
	-96,246	47,719	-97,859	9,11E-04
	-100,113	47,284	-98,830	7,49E-04
	-93,059	53,005	-94,869	3,87E-03
	-95,602	54,669	-98,444	4,41E-04
	-104,855	42,729	-99,922	9,13E-03
	-95,770	53,844	-98,526	5,38E-04
	-96,384	49,737	-98,253	1,65E-04
	-100,838	48,287	-97,428	6,10E-05
	-94,046	52,555	-97,784	5,75E-05
	-87,110	58,060	-97,878	3,33E-04

B.3. Minimization of the distances

Table B.3.1. –20 optimizations and respective final value of the objective function *Fval* for the five poses when using idealized dual fluoroscopic images for minimization of the distances under the range of $[\pm 20\,mm;\ \pm 20\,°]$.

	α (°)	β (°)	γ (°)	x (mm)	y (mm)	z (mm)	*Fval*
SP1	0,013	0,019	0,045	0,000	0,003	0,000	3,02E-04
	-0,002	-0,001	-0,007	0,000	-0,001	0,000	4,41E-06
	0,005	0,004	0,033	0,000	0,002	0,001	3,59E-05
	0,000	-0,001	-0,001	0,000	0,000	0,000	1,50E-06
	0,000	0,008	0,045	0,001	0,001	-0,001	5,36E-05
	0,036	0,013	0,034	-0,001	0,005	-0,001	1,15E-03
	0,002	0,023	0,048	-0,002	0,003	0,000	2,80E-04
	0,005	-0,001	0,004	0,000	0,001	0,000	2,59E-05
	0,004	0,007	0,029	0,000	0,002	0,002	4,02E-05
	0,001	0,007	0,029	-0,001	0,002	0,001	3,04E-05
	0,001	0,001	0,007	0,000	0,000	0,000	1,87E-06
	0,006	0,003	0,020	0,001	0,000	0,000	3,52E-05
	0,001	0,000	0,001	0,000	0,000	0,000	1,20E-06
	0,014	0,000	0,024	0,000	0,002	0,000	1,79E-04
	0,004	0,003	0,013	0,000	0,001	0,000	1,50E-05
	0,001	0,040	0,049	-0,004	0,002	0,000	1,01E-03
	0,005	0,007	0,026	0,000	0,001	0,000	4,02E-05
	0,011	0,000	0,012	0,000	0,002	0,000	9,67E-05
	0,000	0,007	0,012	0,000	0,001	0,000	2,71E-05
	0,051	0,020	0,023	-0,002	0,008	-0,002	2,47E-03
SP2	59,705	0,002	0,003	0,000	0,000	-0,002	3,34E-04
	59,690	0,004	0,008	0,000	0,000	0,001	1,61E-05
	59,693	0,001	-0,010	0,000	0,001	-0,001	3,10E-05
	59,691	0,001	0,005	0,000	0,000	0,000	3,21E-06
	59,691	0,001	0,001	0,000	0,000	0,000	1,20E-06
	59,732	0,012	0,068	0,003	0,002	-0,005	3,05E-03
	59,692	0,002	-0,002	0,001	0,000	0,002	2,64E-05
	59,706	0,029	0,053	0,000	0,001	-0,002	1,14E-03
	59,695	0,007	0,024	0,000	0,001	-0,001	9,96E-05
	59,733	0,001	0,023	0,000	0,001	-0,005	2,83E-03
	59,695	0,001	-0,004	0,001	0,000	0,000	3,71E-05
	59,687	0,000	-0,010	0,001	-0,001	0,001	2,99E-05
	59,719	-0,006	0,012	0,004	0,001	-0,003	1,33E-03
	59,677	0,010	0,017	0,000	0,001	0,000	3,77E-04
	59,698	0,015	0,018	0,000	0,000	-0,001	2,92E-04
	59,682	0,001	0,013	0,001	-0,001	0,001	1,21E-04
	59,686	0,005	0,013	0,000	0,000	0,000	6,49E-05
	59,690	0,003	0,002	0,000	0,000	0,000	1,00E-05
	59,694	0,000	0,001	0,000	0,000	0,000	1,88E-05
	59,701	-0,001	0,005	0,000	0,000	-0,001	1,70E-04
SP3	29,847	0,003	0,002	0,000	0,000	0,000	9,80E-06
	29,834	0,022	-0,003	-0,004	0,002	0,000	5,61E-04
	29,846	0,033	0,012	-0,005	0,000	0,002	8,67E-04
	29,847	-0,006	-0,011	0,001	0,001	0,000	3,08E-05
	29,847	0,089	0,029	-0,014	0,000	-0,001	6,33E-03
	29,840	0,017	-0,001	-0,002	0,003	-0,003	3,42E-04
	29,842	0,032	0,012	-0,005	0,000	0,001	8,26E-04
	29,852	0,003	0,000	-0,001	0,001	-0,002	6,54E-05
	29,843	-0,027	-0,047	-0,006	0,001	-0,001	5,65E-04
	29,833	0,248	0,175	-0,038	0,001	0,001	4,63E-02
	29,854	-0,008	0,012	0,001	0,001	-0,001	1,38E-03
	29,828	0,344	0,265	-0,063	0,000	0,000	8,43E-02
	29,827	0,016	0,020	-0,001	0,006	0,000	1,89E-03
	29,839	-0,006	-0,012	0,001	-0,001	0,001	7,63E-05
	29,802	0,158	0,179	-0,021	-0,004	0,004	2,13E-02
	29,844	-0,019	-0,072	0,000	-0,001	0,001	3,31E-04
	29,846	0,027	0,009	-0,005	0,000	0,000	6,00E-04
	29,884	-0,003	-0,036	-0,002	0,008	-0,006	4,37E-03
	29,840	0,041	0,012	-0,007	0,001	-0,001	1,36E-03
	29,821	0,245	0,210	-0,038	-0,001	0,002	4,48E-02
RGP1	99,540	-38,326	-109,997	7,897	-11,611	12,412	7,92E-05
	99,331	-38,484	-109,879	7,892	-11,606	12,408	5,90E-03
	99,570	-38,294	-109,981	7,897	-11,609	12,412	6,55E-04
	100,495	-37,441	-110,345	7,915	-11,597	12,456	1,15E-01
	99,684	-38,219	-110,021	7,899	-11,614	12,412	2,96E-03
	99,848	-38,071	-110,114	7,903	-11,614	12,421	1,30E-02
	99,820	-38,067	-110,115	7,906	-11,606	12,425	1,24E-02
	99,650	-38,237	-110,009	7,899	-11,609	12,413	1,86E-03
	99,538	-38,335	-110,004	7,896	-11,611	12,412	7,08E-06
	99,474	-38,381	-109,959	7,894	-11,610	12,410	6,22E-04
	99,856	-38,057	-110,122	7,903	-11,612	12,422	1,36E-02
	99,710	-38,219	-110,026	7,899	-11,615	12,403	5,47E-03
	99,616	-38,261	-110,008	7,897	-11,611	12,412	8,91E-04
	99,436	-38,435	-109,980	7,899	-11,611	12,417	1,51E-03
	99,557	-38,318	-110,014	7,897	-11,611	12,412	6,91E-05
	99,572	-38,320	-110,022	7,895	-11,616	12,410	2,73E-04
	99,594	-38,281	-110,017	7,896	-11,610	12,413	3,95E-04
	99,607	-38,326	-110,038	7,899	-11,623	12,408	3,04E-03
	99,837	-38,040	-110,088	7,903	-11,605	12,423	1,41E-02
	99,658	-38,229	-110,007	7,899	-11,609	12,412	2,21E-03
RGP2	-93,352	53,594	-98,011	14,733	8,698	17,319	2,74E-04
	-92,827	54,132	-97,959	14,734	8,698	17,319	1,19E-04
	-92,784	54,180	-97,923	14,731	8,699	17,319	1,17E-03
	-92,351	54,618	-97,917	14,738	8,698	17,320	2,84E-03
	-88,962	58,009	-97,675	14,753	8,677	17,317	7,75E-02
	-91,696	55,283	-97,848	14,739	8,698	17,320	6,71E-03
	-93,365	53,587	-98,004	14,733	8,700	17,319	2,85E-04
	-89,930	57,132	-97,673	14,744	8,708	17,310	4,86E-02
	-93,557	53,389	-98,035	14,731	8,698	17,318	5,68E-04
	-88,237	58,782	-97,555	14,752	8,683	17,313	1,13E-01
	-92,673	54,285	-97,927	14,734	8,696	17,319	7,59E-04
	-92,929	54,029	-97,978	14,736	8,697	17,319	1,69E-05
	-90,752	56,237	-97,753	14,741	8,692	17,318	2,64E-02
	-92,664	54,284	-97,944	14,734	8,698	17,320	5,61E-04
	-91,614	55,366	-97,820	14,737	8,698	17,321	8,33E-03
	-91,706	55,274	-97,809	14,733	8,697	17,320	8,77E-03
	-93,693	53,241	-98,042	14,729	8,700	17,320	1,03E-03
	-91,255	55,735	-97,770	14,737	8,699	17,319	1,73E-02
	-91,155	55,780	-97,784	14,741	8,691	17,325	1,92E-02
	-91,261	55,727	-97,790	14,739	8,698	17,319	1,55E-02

C. Idealized single fluoroscopic images

C.1. Range of $\pm 5\ mm$ in translation and $\pm 5\ °$ in rotation

Table C.1.1. –20 optimizations and respective final value of the objective function *Fval* for the five poses when using idealized single fluoroscopic images for minimization of the distances under the range of $[\pm 5\ mm;\ \pm 5\ °]$.

	α (°)	β (°)	γ (°)	x (mm)	y (mm)	z (mm)	*Fval*
SP1	0,007	0,006	0,026	-0,001	0,457	-0,001	1,40E-05
	0,082	-0,002	0,015	0,000	-4,227	-0,002	1,92E-04
	-0,009	0,011	0,055	0,000	3,115	0,000	3,50E-05
	0,000	0,005	0,027	0,000	2,090	0,000	8,60E-06
	0,053	-0,009	-0,067	0,000	1,798	-0,002	1,13E-04
	0,001	0,001	0,004	0,000	-1,741	0,000	2,79E-07
	0,037	0,005	0,024	0,000	-3,170	-0,001	4,19E-05
	0,022	0,002	0,015	0,000	-1,950	-0,001	1,44E-05
	-0,010	0,006	0,027	-0,001	1,443	0,000	1,38E-05
	0,003	0,003	0,022	0,000	-4,538	0,000	4,49E-06
	-0,001	0,011	0,048	-0,001	0,565	0,000	3,70E-05
	0,004	0,000	0,001	0,000	-2,434	0,000	4,85E-07
	-0,049	0,008	0,069	0,001	1,888	0,001	1,04E-04
	-0,001	0,008	0,052	0,000	3,150	0,000	2,35E-05
	-0,046	0,026	0,068	-0,002	3,087	0,001	3,17E-04
	0,001	-0,001	-0,002	0,000	1,515	0,000	3,98E-07
	-0,039	0,013	0,064	0,000	-1,536	0,001	9,02E-05
	0,005	0,006	0,025	-0,001	-4,016	0,000	9,75E-06
	-0,006	0,014	0,043	-0,001	2,363	0,000	7,78E-05
	-0,011	0,006	0,037	0,000	-1,268	0,000	1,57E-05
SP2	59,685	0,000	0,005	0,000	-3,235	0,000	2,25E-05
	59,692	0,005	0,009	0,000	3,386	0,000	2,14E-05
	59,690	0,003	0,008	0,000	-0,698	0,000	1,12E-05
	59,711	-0,024	0,032	0,000	-2,786	-0,002	9,90E-04
	59,695	0,000	0,002	0,000	1,533	0,000	1,88E-05
	59,694	-0,001	-0,002	0,000	3,938	0,000	1,08E-05
	59,690	0,000	0,001	0,000	-1,244	0,000	3,25E-07
	59,690	-0,006	0,011	0,001	0,049	0,000	4,91E-05
	59,690	0,000	0,000	0,000	4,450	0,000	5,44E-08
	59,691	-0,006	-0,004	-0,001	-3,352	0,001	3,00E-05
	59,691	0,009	0,006	0,001	-0,992	0,000	6,26E-05
	59,690	0,001	0,003	0,000	1,321	0,000	1,06E-06
	59,702	0,006	0,006	0,000	2,293	-0,001	1,27E-04
	59,695	0,001	0,003	0,000	-3,569	-0,001	2,06E-05
	59,690	0,003	0,002	0,000	0,559	0,000	5,83E-06
	59,694	0,001	0,003	0,000	2,533	0,000	1,17E-05
	59,689	0,004	0,003	0,000	3,138	0,000	1,23E-05
	59,697	0,044	0,043	-0,002	4,407	-0,001	1,58E-03
	59,694	0,023	0,022	-0,002	-2,438	0,000	4,54E-04
	59,695	-0,001	0,028	0,003	-4,584	0,000	8,78E-05
SP3	29,848	0,005	0,037	0,001	2,712	0,000	4,04E-05
	29,844	0,010	0,033	0,000	-1,380	0,000	7,01E-05
	29,845	0,002	0,004	0,000	4,009	0,001	3,82E-06
	29,861	0,015	0,038	-0,001	-2,271	-0,002	2,12E-04
	29,841	0,000	-0,002	0,000	-4,581	0,001	6,78E-06
	29,846	0,007	0,015	0,000	-0,093	0,000	3,11E-05
	29,834	0,004	-0,010	0,000	2,012	0,001	6,34E-05
	29,850	0,053	0,126	-0,004	-3,560	-0,001	1,85E-03
	29,856	0,001	0,007	0,001	4,067	-0,002	3,91E-05
	29,856	-0,003	-0,004	0,000	1,523	-0,001	4,01E-05
	29,849	0,018	0,108	0,002	-0,489	-0,001	3,70E-04
	29,846	0,006	0,019	0,000	-2,393	0,000	2,53E-05
	29,848	0,052	0,120	-0,003	-1,674	-0,001	1,76E-03
	29,846	0,010	0,026	-0,001	2,361	0,000	7,24E-05
	29,843	0,002	0,015	0,001	-4,789	0,001	9,14E-06
	29,847	0,007	0,033	0,000	2,242	0,000	4,45E-05
	29,852	0,001	0,012	0,001	-2,827	-0,001	1,64E-05
	29,858	0,001	0,003	0,000	-2,423	-0,001	4,95E-05
	29,845	0,016	0,033	0,000	0,782	0,000	1,78E-04
	29,851	-0,008	-0,002	0,000	0,323	-0,001	5,82E-05
RGP1	99,655	-38,203	-110,040	7,899	-16,171	12,420	1,27E-03
	99,559	-38,308	-110,007	7,896	-9,586	12,412	3,98E-05
	99,505	-38,363	-109,981	7,895	-10,659	12,410	6,64E-05
	99,767	-38,130	-110,087	7,902	-7,458	12,423	2,69E-03
	99,659	-38,202	-110,043	7,901	-12,352	12,426	1,29E-03
	99,864	-37,951	-110,092	7,908	-11,092	12,435	7,08E-03
	99,624	-38,306	-110,176	7,908	-7,907	12,438	9,65E-03
	99,447	-38,420	-109,957	7,894	-13,314	12,406	3,59E-04
	99,843	-38,049	-110,115	7,905	-13,174	12,431	4,22E-03
	99,532	-38,341	-109,998	7,895	-15,006	12,411	1,99E-06
	99,660	-38,218	-110,025	7,899	-8,952	12,417	7,28E-04
	99,578	-38,292	-110,015	7,897	-7,585	12,414	7,30E-05
	99,424	-38,446	-109,944	7,893	-8,765	12,405	6,04E-04
	99,516	-38,356	-109,990	7,896	-11,578	12,408	2,68E-05
	99,927	-37,972	-110,161	7,907	-6,675	12,435	6,46E-03
	99,699	-38,184	-110,061	7,899	-7,199	12,421	1,57E-03
	99,991	-37,863	-110,166	7,907	-12,625	12,441	9,31E-03
	99,785	-38,050	-110,103	7,904	-16,451	12,430	4,09E-03
	99,538	-38,337	-110,001	7,896	-10,045	12,411	5,62E-07
	99,499	-38,367	-109,987	7,895	-8,868	12,410	6,57E-05
RGP2	-93,570	53,375	-98,038	14,731	12,532	17,321	2,90E-04
	-93,590	53,351	-98,033	14,732	11,528	17,320	2,73E-04
	-93,562	53,382	-98,034	14,733	8,703	17,320	2,56E-04
	-90,139	56,957	-97,756	14,750	13,384	17,306	1,24E-02
	-93,052	53,905	-97,985	14,734	12,788	17,319	1,53E-06
	-91,142	55,879	-97,828	14,744	11,668	17,312	7,82E-03
	-92,081	54,804	-97,919	14,738	6,140	17,324	2,29E-03
	-92,343	54,579	-97,932	14,737	11,727	17,321	8,20E-04
	-92,379	54,547	-97,923	14,736	11,882	17,321	7,72E-04
	-92,423	54,505	-97,938	14,737	12,775	17,321	5,94E-04
	-93,177	53,774	-97,997	14,734	13,159	17,319	1,93E-05
	-90,070	57,003	-97,740	14,749	9,676	17,307	1,24E-02
	-92,804	54,159	-97,962	14,735	5,940	17,318	3,68E-05
	-93,006	53,958	-97,980	14,735	6,553	17,318	9,58E-06
	-93,347	53,616	-98,004	14,733	12,743	17,320	1,61E-04
	-91,920	55,074	-97,893	14,741	9,549	17,320	2,67E-03
	-91,424	55,509	-97,850	14,741	12,426	17,322	4,46E-03
	-91,696	55,295	-97,890	14,742	6,269	17,318	3,24E-03
	-90,966	56,052	-97,814	14,745	12,502	17,310	8,33E-03
	-92,743	54,221	-97,959	14,735	8,145	17,318	5,11E-05

C.2. Range of $\pm 20\ mm$ in translation and $\pm 20\ °$ in rotation

Table C.2.1. –20 optimizations and respective final value of the objective function *Fval* for the five poses when using idealized single fluoroscopic images for minimization of the distances under the range of $[\pm 20\ mm;\ \pm 20\ °]$.

	α (°)	β (°)	γ (°)	x (mm)	y (mm)	z (mm)	*Fval*
SP1	-0,020	0,095	0,154	-0,008	-13,793	-0,001	6,10E-03
	-0,001	0,002	0,015	0,000	0,106	0,000	2,15E-06
	0,006	0,004	0,018	0,000	13,604	0,000	4,56E-06
	0,004	0,002	0,018	0,000	8,872	0,000	3,29E-06
	0,002	0,007	0,037	0,000	4,099	0,000	1,45E-05
	-0,039	0,002	0,066	0,000	-1,719	0,001	1,22E-04
	-0,038	0,015	0,065	0,001	-8,772	0,001	9,99E-05
	-0,045	0,011	0,057	0,000	-5,641	0,002	9,06E-05
	0,005	0,000	-0,002	0,000	19,008	0,000	7,96E-07
	-0,002	-0,005	-0,025	0,000	-0,918	-0,001	8,58E-06
	0,007	0,007	0,041	0,000	-14,859	0,000	1,64E-05
	0,001	0,007	0,032	0,000	14,740	0,000	1,28E-05
	-0,003	0,011	0,051	0,000	-10,496	0,000	3,59E-05
	-0,002	0,006	0,016	-0,001	7,790	0,000	1,17E-05
	0,007	0,000	0,002	0,000	19,369	0,000	1,29E-06
	-0,005	0,003	-0,018	0,000	-16,844	0,000	3,41E-05
	-0,039	0,008	0,064	0,001	-19,042	0,001	7,70E-05
	-0,040	0,009	0,064	0,000	1,205	0,001	7,58E-05
	-0,002	0,012	0,052	0,000	-12,511	0,000	4,42E-05
	-0,048	0,019	0,068	0,002	13,071	0,001	1,82E-04
SP2	59,690	0,014	0,011	0,000	-16,235	0,000	1,58E-04
	59,690	0,013	0,008	0,005	3,823	0,001	1,68E-04
	59,691	-0,006	0,017	-0,001	-18,287	0,000	7,79E-05
	59,703	0,006	0,005	0,000	1,570	-0,001	1,49E-04
	59,688	0,000	0,005	0,000	-16,747	0,000	5,24E-06
	59,716	0,008	0,012	0,001	10,269	-0,002	5,38E-04
	59,697	0,000	0,003	0,000	19,767	-0,001	3,69E-05
	59,690	0,006	0,005	0,000	-16,881	0,000	3,46E-05
	59,691	-0,002	0,000	0,000	-7,017	0,000	2,99E-06
	59,697	-0,001	0,002	0,000	-0,783	-0,001	3,12E-05
	59,681	0,004	-0,018	-0,001	-14,503	0,001	1,08E-04
	59,689	0,007	0,006	0,000	18,255	0,000	3,82E-05
	59,691	0,005	-0,001	-0,001	17,076	0,000	2,20E-05
	59,690	0,002	0,001	0,000	3,787	0,000	3,94E-06
	59,692	0,003	0,013	0,000	8,344	0,000	1,75E-05
	59,690	0,002	0,004	0,000	-13,935	0,000	4,51E-06
	59,691	0,012	0,015	0,000	3,494	0,000	1,23E-04
	59,692	0,006	0,009	-0,001	-9,671	0,001	3,24E-05
	59,712	0,001	0,004	0,000	9,101	-0,002	3,31E-04
	59,699	0,011	0,012	0,000	18,835	-0,001	1,57E-04
SP3	29,845	0,000	-0,001	0,000	0,000	0,000	4,29E-05
	29,845	0,000	-0,001	0,000	0,000	0,000	8,89E-05
	29,843	-0,088	-0,166	-0,020	0,002	0,000	2,10E+00
	29,848	0,010	0,004	-0,002	0,000	0,000	1,94E-02
	29,845	0,000	-0,003	0,000	0,000	0,000	1,56E-04
	29,845	0,042	0,015	-0,007	0,000	0,000	3,12E-01
	29,849	0,001	0,000	0,000	0,001	-0,001	6,01E-03
	29,845	0,006	0,003	-0,001	0,000	0,000	7,36E-03
	29,847	-0,002	-0,008	0,000	0,000	0,000	1,95E-03
	29,845	0,005	-0,001	-0,001	0,000	0,000	5,43E-03
	29,845	-0,006	-0,005	0,001	0,000	0,000	5,41E-03
	29,845	0,013	0,005	-0,002	0,000	0,000	2,83E-02
	29,845	0,000	0,000	0,000	0,000	0,000	2,72E-06
	29,845	0,001	0,001	0,000	0,000	0,000	8,41E-05
	29,846	-0,001	-0,005	0,000	0,000	0,000	8,89E-04
	29,845	0,001	0,001	0,000	0,000	0,000	1,00E-04
	29,846	0,002	0,002	0,000	0,000	0,000	7,41E-04
	29,846	0,014	0,005	-0,002	0,000	0,000	3,37E-02
	29,847	-0,001	0,000	0,000	0,000	0,000	1,32E-03
	29,846	0,000	-0,071	-0,003	0,000	0,001	2,63E-01
RGP1	99,593	-38,277	-110,023	7,897	-6,645	12,417	1,38E-04
	99,821	-37,993	-110,076	7,906	-4,635	12,436	6,00E-03
	95,165	-55,542	-109,886	10,044	-13,834	15,245	1,24E+00
	100,877	-37,089	-110,551	7,916	-1,560	12,474	7,28E-02
	99,624	-38,245	-110,032	7,898	-0,820	12,416	3,13E-04
	100,096	-37,874	-110,232	7,907	-8,701	12,438	1,33E-02
	99,473	-38,389	-109,960	7,893	-29,770	12,408	2,93E-04
	99,549	-38,326	-110,005	7,896	-3,756	12,412	4,27E-06
	100,994	-36,642	-110,361	8,048	-25,858	12,566	1,41E-01
	102,671	-35,189	-111,506	8,107	-25,098	12,725	3,16E-01
	99,499	-38,328	-109,914	7,895	-2,633	12,411	2,64E-03
	110,647	-58,228	-114,312	13,176	-4,121	20,118	2,58E+00
	99,663	-38,207	-110,052	7,899	4,891	12,420	1,22E-03
	99,705	-38,213	-110,068	7,900	5,803	12,422	1,34E-03
	99,510	-38,361	-109,999	7,894	-16,460	12,410	5,64E-05
	100,062	-37,792	-110,194	7,908	-9,750	12,448	1,49E-02
	99,403	-38,452	-109,931	7,895	-7,104	12,405	8,73E-04
	99,949	-37,888	-110,151	7,907	7,363	12,440	8,46E-03
	95,156	-55,540	-109,886	10,044	1,917	15,245	1,23E+00
	99,578	-38,284	-110,000	7,902	-2,253	12,414	2,37E-04
RGP2	-92,751	54,211	-97,958	14,735	28,481	17,318	5,38E-05
	-89,962	57,105	-97,720	14,748	-9,695	17,307	1,31E-02
	-93,104	53,850	-97,992	14,735	-3,041	17,320	8,42E-06
	-90,954	56,077	-97,806	14,742	16,273	17,311	8,42E-03
	-88,533	58,614	-97,635	14,759	28,455	17,299	2,86E-02
	-92,618	54,333	-97,950	14,735	3,226	17,320	1,58E-04
	-93,523	53,420	-98,031	14,732	14,407	17,320	2,30E-04
	-86,652	60,653	-97,490	14,769	22,358	17,251	6,35E-02
	-93,638	53,302	-98,043	14,731	-0,367	17,320	3,27E-04
	-87,203	60,143	-97,526	14,771	27,532	17,250	5,81E-02
	-93,732	53,226	-98,057	14,731	13,047	17,320	5,53E-04
	-91,761	55,226	-97,879	14,741	15,831	17,318	2,91E-03
	-93,750	53,207	-98,051	14,730	11,221	17,321	4,81E-04
	-91,710	55,283	-97,851	14,739	-7,442	17,318	3,35E-03
	-93,311	53,664	-97,999	14,733	8,695	17,321	2,14E-04
	-86,833	60,453	-97,494	14,771	21,937	17,253	6,17E-02
	-84,034	63,488	-97,293	14,778	3,279	17,211	1,10E-01
	-93,236	53,715	-98,000	14,733	-2,698	17,319	3,85E-05
	-88,056	59,128	-97,591	14,765	21,973	17,301	4,00E-02
	-86,689	60,605	-97,486	14,772	-2,399	17,253	6,32E-02